Title

Computational Interpretation and Design of Molecular Probe Characterization Techniques for Lewis Acid Zeolites

Author

Holton, Sam J

Publication Date

2023

Peer reviewed|Thesis/dissertation

Computational Interpretation and Design of Molecular Probe Characterization Techniques for Lewis Acid Zeolites

By

Sam J. Holton
DISSERTATION

Submitted in partial satisfaction of the requirements for the degree of

DOCTOR OF PHILOSOPHY

in

Materials Science and Engineering

in the

OFFICE OF GRADUATE STUDIES

of the

UNIVERSITY OF CALIFORNIA

DAVIS

Approved:

Ambarish Kulkarni, Chair

Ron Runnebaum

Nir Goldman

Committee in Charge

2023

Abstract

Zeolites are nanoporous, aluminosilicate materials commonly used as catalysts in the chemical industry. The addition of metal atoms gives zeolites a wide range of catalytic activities while synthesis conditions can control the hydrophobicity, size, and shape of the pores. To aid computational studies of zeolites, we developed software to streamline the preparation of atomic structures for simulations. In conjunction with density functional theory calculations, these capabilities are employed to study Sn/Ti catalysts on silica for the Henry reaction. Next, I study Lewis-acidic tin zeolites of interest for biomass conversion and pharmaceutical production. The tin atom can be found in closed, hydrolyzed open, and open defect configurations, each with distinct catalytic properties. Computational studies of Sn-BEA for the epichlorohydrin ring opening reaction demonstrate the effect of active site speciation on turnover frequency. Active site characterization is challenging in tin zeolites, which limits our understanding of their catalytic properties and makes it difficult to improve synthetic techniques. To address this, we use high-throughput DFT calculations and experiments to validate TMPO as a ^{31}P NMR probe that can distinguish open defect and closed sites in BEA. We use a similar approach to study acetonitrile ^{15}N NMR probes, which can distinguish closed, hydrolyzed open, and open defect sites in Chabazite. These new techniques will improve zeolite characterization and accelerate catalyst development.

Dedicated to my fiancée, Rachel

Table of Contents

Introduction

Zeolite Catalysts

Zeolites are structurally diverse nanoporous frameworks with an SiO2 stoichiometry. Typical pore sizes closely match the size of common organic molecules which makes zeolites well suited for size selective catalysis. Additionally, zeolites are stable in a wide range of temperatures and reaction conditions. These properties make zeolites well suited for catalysis across the petrochemical industry [2]. One reaction which zeolites are particularly useful for is fluid catalytic cracking, where heavy hydrocarbon fractions of oil are broken down into smaller hydrocarbons to make precursors for important chemical products.

Because zeolites have been used in industry and research for decades, designing the zeolite pore structure and catalytic activity is well understood. Zeolite hydrothermal synthesis conditions can be adjusted to achieve different pore structures and different Si/Al ratios while structure directing agents can be added during synthesis to change the shape of the pore network [3]. To change catalytic activity, atoms such as Ga, B, Ti, Sn, and Pt can be inserted into the framework [4] or encapsulated as nanoclusters [5].

In the past, attempts have been made to design zeolites for chiral and regioselective catalysis by leveraging these synthetic techniques. These include designing syntheses to generate enantiomerically enriched zeolites such as BEA [1] (see figure 1), anchoring organometallic chiral catalysts6, and encapsulating enzymes into a zeolite framework [7].

With various potential structures and many possible synthetic modifications of zeolites, a significant amount of computational work has explored zeolite catalyst design. A first step towards designing zeolites enumerated 2.7 million possible zeolite structures [8]. Progress is also being made to automatically read literature and predict new zeolite syntheses [9]. Other work has attempted to computationally design organic structure directing agents [10]. Designing zeolite active sites becomes a natural complement to this previous work.

Structure of the Dissertation

The remainder of the dissertation is structured as follows. The background chapter will detail the relevant techniques used in this work; illustrating how DFT can be used to estimate the thermodynamic and kinetic properties of a catalyst as well as interpret IR and NMR characterization techniques. Chapter 1 will discuss the functionalities of the Multiscale Atomistic Zeolite simulation Environment (MAZE) code; this software is used to facilitate research in future chapters. Chapter 2 details a case study in understanding a Sn-silica catalyst for the Henry reaction, illustrating some important themes in experimental and theoretical collaboration for chapters to follow. Chapter 3 turns to the main thrust of the remainder of the dissertation, the study and characterization of tin speciations in zeolites, using epichlorohydrin ring opening as a representative reaction. Chapter 4 approaches this characterization problem from a different perspective, assessing the ability of tri-methyl phosphine oxide (TMPO) to identify Sn site speciation in BEA. Finally, Chapter 5 applies these techniques to the problem of using acetonitrile probes to characterize tin sites in Chabazite. The conclusion considers these themes in more detail and suggests some avenues for further research.

Background

Density Functional Theory

Chemical reactions are fundamentally a quantum mechanical process. As such, a detailed understanding of catalytic processes and catalyst design requires an understanding of the quantum mechanical motions of atoms about the active site. While quantum mechanics is well described by solutions to the Schrodinger equation, solving this equation for the many electron systems of interest in catalysis is intractable even on modern computers. Given this, many different computational approaches are used; these methods result in trade offs between accuracy and computational costs. For example, CCSD(T) is often used as a "gold standard" with high accuracy but with $O(n^7)$ scaling in the number of electrons [15]. On the other hand, molecular dynamics simulations (based on classical force fields) can offer sub-quadratic scaling in the number of atoms, at the cost of higher errors [16]. However, arguably the most successful method in quantum chemistry to date is density functional theory (DFT). DFT offers $O(n^3)$ scaling in the number of electrons with 0.2-0.4 eV error for a wide range of chemical systems [17]. DFT does away with probability amplitudes for each electron across space and uses a total density at each point instead. DFT is based on two theorems. The first Hohenberg-Kohn theorem states that any ground state property of a system is uniquely determined by an electron density, which reduces the degrees of freedom from 3N to 3. The second Hohenberg-Kohn theorem states that for any system, the correct electron density is the one which minimizes an energy functional based on the system's Hamiltonian. This functional has the following form:

$$E[\rho] = T_s[\rho] + \int d\mathbf{r}\, v_{\text{ext}}(\mathbf{r})\rho(\mathbf{r}) + E_H[\rho] + E_{\text{xc}}[\rho]$$

Where $T_s[\rho]$ is the kinetic energy, $E_H[\rho]$ represents the Coulomb repulsion, and $E_{XC}[\rho]$ is the exchange-correlation functional. Unfortunately the exchange-correlation functional is not known, rather, it must be approximated [18]. $E_{XC}[\rho]$ can be approximated in many ways, and decades of work have been spent designing suitable approximations for different situations. For this work, I will use the RPBE functional, which is a re-parameterization of the popular PBE functional that produces more accurate adsorption energies [19]. Additionally, I will be using the Vienna Ab Initio Simulation Package (VASP) for calculations. This program uses smooth approximations of the wavefunctions of the core electrons, called psudo-potentials, to speed up calculations.

Referencing Energies

In order to appropriately compare the energies of different species, energies derived from DFT must be referenced so that only systems with the same number of atoms (and calculated using hte same functional) are compared to one another. The difference in energy between two systems with the same number and types of atoms can then be attributed to differences in their spatial arrangement. For example, the energy of a molecule bound to a metal surface could be compared to the total energy of a bare surface and a gas phase molecule.

The difference between these two energies can be attributed to the binding interaction between the molecule and the metal surface. Subtracting the gas phase and bare metal energies from the energy of the combined system represents the energy of the bonding interaction, often referred to as the binding energy. It is critical for the reference species to be as similar as possible to the system under study. For instance, referencing the energy of a hydrocarbon to an equiatomic

mixture of carbon and hydrogen gas obscures how different bonds contribute to the overall energy. As much as possible, methods for referencing energies in this work will pinpoint the binding energy associated with individual bonds of interest, often between a molecule and the Lewis-acid site.

Energy Barrier Calculations

Barrier calculations are essential for understanding catalytic activity; the free energy barrier of a reaction determines the turnover frequency of a catalyst. The energy barrier for a reaction is determined by the lowest first-order transition state connecting the basin of the initial state to the final state. Finding a transition state is significantly harder than optimizing the geometry, however, several methods exist to find this transition state such as Nudged Elastic Band and growing string methods [23] . We chose to use Climbing Image Nudged Elastic Band calculations to find the transition state [20] in these studies.

Harmonic Vibrational Analysis and Infrared Spectroscopy

DFT can be used to compute the vibrational modes of atoms in a molecule, which is useful for predicting frequencies in IR spectroscopy or computing harmonic free energies. Following the derivations from Sholl and Steckel [22], This is done by using a harmonic approximation. For a bond at equilibrium, the energy of small displacements d away from the equilibrium position x_0 can be approximated with a Taylor series:

$$E(x_0 + d) \approx E(x_0) + \frac{1}{2}\frac{d^2E}{dx^2}(d - x_0)^2$$

where $E(x_0)$ is the equilibrium energy. The first-order term is approximately zero due to the assumption that the system is at a potential minimum. Generalizing this to collections of atoms and general displacements, the equation of motion for the system can be written in matrix form as:

$$\frac{d^2x}{dt^2} = Ax$$

where x is the equilibrium displacement vector and A is the mass-weighted Hermitian matrix ($A_{ij} = H_{ij} / m_i$). This differential equation has solutions that are linear combinations of the eigenvectors (or normal modes) of A.

Note that DFT calculations alone are not sufficient to compute the Hessian matrix, and the matrix elements are approximated using finite difference methods:

$$H_{ij} \approx \frac{E(\delta x_i, \delta x_j) + 2E_0 + E(-\delta x_i, -\delta x_j)}{\delta x_i \delta x_j}$$

Where $E(\delta x_i, \delta x_j)$ denotes a small displacement of coordinates i and j with the other coordinates held fixed.

For our purposes, many of the normal modes of an atomic system often correspond to familiar bond vibrations studied in infrared spectroscopy. The eigenvalues of these normal modes can be converted into frequencies and compared to frequencies obtained from infrared spectroscopy.

Often, these frequencies are in error by roughly 20 cm^{-1} (compared to experiments) but can still provide useful trends and insight.

Harmonic Free Energy Calculations

With harmonic vibrational analysis, the calculation of useful quantities can be undertaken. The enthalpy of a chemical system can be computed by $H = U(T) + pV$ where $U(T)$ can be computed via:

$$U(T) = E_{\text{elec}} + E_{\text{ZPE}} + \sum_{i}^{\text{harm DOF}} \frac{\epsilon_i}{e^{\epsilon_i/k_B T} - 1}$$

In solids, the pV work, translational energy, and rotational energy are assumed to be negligible, simplifying the calculation of enthalpy. The zero point energy and vibrational energy terms are computed using the normal modes discussed in the previous section. Using this harmonic potential, the zero point energy is the lowest energy state of a quantum simple harmonic oscillator. The vibrational entropy can then be computed by:

$$S = k_B \sum_{i}^{\text{harm DOF}} \left[\frac{\epsilon_i}{k_B T \left(e^{\epsilon_i/k_B T} - 1 \right)} - \ln\left(1 - e^{-\epsilon_i/k_B T}\right) \right]$$

where ε_i refers to the energy of the i^{th} vibrational energy level.

Assuming the pV work is negligible, the free energy of the system is well approximated by the Helmholtz free energy and can be computed as:

$$G(T) \approx F(T) = U(T) - TS(T)$$

Nuclear Magnetic Resonance Spectroscopy

Nuclear Magnetic Resonance (NMR) spectroscopy is a well-developed technique for identifying the structure of molecules and solids. It usually relies on the presence of spin-1/2 nuclei such as ^{1}H, ^{19}F, or ^{31}P.

NMR spectroscopy works by applying a magnetic field to a sample, which causes nuclear spins in the sample to precess about this magnetic field. The applied field creates a split in the energy levels of the spin up and spin down states, and creates a slight polarization of the spin up state. Next, a radio-frequency pulse (chosen based on the nuclei of interest and the magnitude of the applied field) is applied to the sample perpendicular to the magnetic field. This induces Rabi oscillations between the two spin states, and the pulse length is chosen to make the nuclear spin precess in a plane perpendicular to the direction of the external magnetic field. Each nucleus responds differently to the radio frequency pulse depending on the electronic environment it is in and precesses at a distinct frequency. These frequencies are measured by a coil of wire around the sample, and the observed signal is Fourier transformed to obtain distinct peaks for each chemically distinct nucleus in the sample. In solid state NMR, two additional parameters can be measured from the sample: the chemical shift anisotropy and the asymmetry parameter, which relate to other properties of the electronic environment around the nucleus.

These three parameters can be computed using DFT. This is done by first computing the components of the chemical shielding tensor, defined as:

$$\sigma_{ij}(R) = -\frac{\partial B^{ind}_{i}(R)}{\partial B^{ext}_{j}}$$

Where R denotes the nucleus of interest, B^{ind} is the induced magnetic field and B^{ext} is the applied magnetic field. In VASP, this tensor is computed using a linear response method [21]. NMR can only measure the symmetric part of this tensor, so it is symmetrized. The tensor is permuted so that $\sigma_{xx} > \sigma_{yy} > \sigma_{zz}$ and this first diagonal value is the chemical shift, the second is the nuclear span, and the third is the skew.

To properly compare to experiment, both theoretical and experimental values are adjusted relative to a reference chemical shift:

$$\sigma = \sigma_{ref} - \sigma(R)$$

Where σ_{ref} is the reference molecule's chemical shift, and $\sigma(R)$ is the raw chemical shift of the nucleus of interest.

References

(1) Davis, M. E. A Thirty-Year Journey to the Creation of the First Enantiomerically Enriched Molecular Sieve. ACS Catal. 8, 10082–10088 (2018).

(2) Vermeiren, W. & Gilson, J. P. Impact of zeolites on the petroleum and petrochemical industry. Top. Catal. 52, 1131–1161 (2009).

(3) Lobo, R. F., Zones, S. I. & Davis, M. E. Structure-direction in zeolite synthesis. J. Incl. Phenom. Mol. Recognit. Chem. 21, 47–78 (1995).

(4) Li, P. et al. Postsynthesis and selective oxidation properties of nanosized Sn-beta zeolite. J. Phys. Chem. C 115, 3663–3670 (2011).

(5) Liu, L. et al. Generation of subnanometric platinum with high stability during transformation of a 2D zeolite into 3D. Nat. Mater. 16, 132–138 (2017).

(6) Corma, A., Iglesias, M., Del Pino, C. & Sánchez, F. New rhodium complexes anchored on modified USY zeolites. A remarkable effect of the support on the enantioselectivity of catalytic hydrogenation of prochiral alkenes. J. Chem. Soc. Chem. Commun. 1253–1255 (1991). doi:10.1039/C39910001253

(7) Carceller, J. M., Mifsud, M., Climent, M. J., Iborra, S. & Corma, A. Production of chiral alcohols from racemic mixtures by integrated heterogeneous chemoenzymatic catalysis in fixed bed continuous operation †. (2020). doi:10.1039/c9gc04127c

(8) Deem, M. W., Pophale, R., Cheeseman, P. A. & Earl, D. J. Computational discovery of new zeolite-like materials. J. Phys. Chem. C 113, 21353–21360 (2009).

(9) Corma, A., Moliner, M. & Roma, Y. Machine Learning Applied to Zeolite Synthesis : The Missing Link for Realizing High-Throughput Discovery. (2019). doi:10.1021/acs.accounts.9b00399

(10) Daeyaert, F., Ye, F. & Deem, M. W. Machine-learning approach to the design of OSDAs for zeolite beta. Proc. Natl. Acad. Sci. 116, 3413–3418 (2019).

(11) Corma, A., Nemeth, L. T., Renz, M. & Valencia, S. Sn-zeolite beta as a heterogeneous chemoselective catalyst for Baeyer-Villiger oxidations. Nature 412, 423–425 (2001).

(12) Deshpande, N. et al. Epoxide ring opening with alcohols using heterogeneous Lewis acid catalysts: Regioselectivity and mechanism. J. Catal. 370, 46–54 (2019).

(13) Stalcup, A. M. Chiral Separations. Annu. Rev. Anal. Chem. 3, 341–363 (2010).

(14) Heitbaum, M., Glorius, F. & Escher, I. Asymmetric heterogeneous catalysis. Angew. Chemie - Int. Ed. 45, 4732–4762 (2006).

(15) Stamper, J. G. A Note on the treatment of Quadruple Excitations in Configuration Interaction. Theor. Chim. Acta. 459–462 (1968). doi:https://doi.org/10.1007/BF00526665

(16) Shan, Y., Klepeis, J. L., Eastwood, M. P., Dror, R. O. & Shaw, D. E. Gaussian split Ewald: A fast Ewald mesh method for molecular simulation. J. Chem. Phys. 122, (2005).

(17) Kohn, W. & Sham, L. J. Self-Consistent Equations Including Exchange and Correlation Effects. Phys. Rev. A 140, 1133–1138 (1965).

(18) Schuch, N. & Verstraete, F. Computational complexity of interacting electrons and fundamental limitations of density functional theory. Nat. Phys. 5, 732–735 (2009).

(19) Hammer, B., Hansen, L. B. & Nørskov, J. K. Improved adsorption energetics within density-functional theory using revised Perdew-Burke-Ernzerhof functionals. Phys. Rev. B - Condens. Matter Mater. Phys. 59, 7413–7421 (1999).

(20) Henkelman, G., Uberuaga, B. P. & Jónsson, H. Climbing image nudged elastic band method for finding saddle points and minimum energy paths. J. Chem. Phys. 113, 9901–9904 (2000).

(21) Yates, J. R.; Pickard, C. J.; Mauri, F. Calculation of NMR Chemical Shifts for Extended Systems Using Ultrasoft Pseudopotentials. *Phys. Rev. B* **2007**, *76* (2), 024401. https://doi.org/10.1103/PhysRevB.76.024401.

(22) DFT Calculations of Vibrational Frequencies. In *Density Functional Theory*; John Wiley & Sons, Ltd, 2009; pp 113–130. https://doi.org/10.1002/9780470447710.ch5.

(23) Peters, B.; Heyden, A.; Bell, A. T.; Chakraborty, A. A Growing String Method for Determining Transition States: Comparison to the Nudged Elastic Band and String Methods. *J. Chem. Phys.* **2004**, *120* (17), 7877–7886. https://doi.org/10.1063/1.1691018.

Chapter 1

Simplifying computational workflows with the Multiscale Atomic Zeolite Simulation Environment (MAZE)

Dexter D. Antonio, Jiawei Guo, Sam J. Holton, Ambarish R. Kulkarni

My contributions to this work consist of developing the code used to extract and cap clusters as well as the code to place adsorbates into the zeolite framework.

Adapted from SoftwareX, Volume 16, 2021, 100797.

Abstract

Zeolites, an important class of 3-dimensional nanoporous materials, have been widely explored for a variety of applications including gas storage, separations, and catalysis. As the properties of these aluminosilicate materials depend on a number of factors (e.g., framework topology, Si/Al ratio, extra-framework cations etc.), detailed experiments (e.g., catalytic properties, adsorption capacities etc.) are often limited to only a handful of materials. Computational methods have played an important role in (1) providing molecular level insights to rationalize experimental observations, and (2) screening large libraries of zeolites to identify promising candidates for experimental synthesis and validation. Different levels of theory and computational chemistry codes are necessary to describe the range of relevant phenomena such as adsorption (e.g., grand canonical Monte Carlo), diffusion (e.g., molecular dynamics), and chemical reactions (e.g., density functional theory). Manipulation of atomic structures, handling of input files, and developing robust workflows becomes quite cumbersome. To mitigate these challenges, we

describe the development of the Multiscale Atomic Zeolite Simulation Environment (MAZE) – a Python package that simplifies zeolite-specific calculation workflows by providing a user-friendly interface for systematically manipulating zeolite structures.

Introduction

Zeolites are a broad class of silica-based nanoporous materials which are widely used for various industrial applications including gas separation and catalysis [1–3]. Transition metal (TM) exchanged zeolites combine the desirable characteristics of heterogeneous catalysts (high thermal stability and simpler separations) with those of enzymes (high selectivity and reactivity under mild conditions) [3] and have received considerable attention as catalysts for numerous reactions, such as NOx abatement [4] and methane valorization [5]. Computational modeling is often used to provide insights (e.g., thermodynamic stabilities [6], reaction barriers [7] etc.) into the reaction mechanisms and properties of zeolites [8,9]. Given the various length- and time-scales associated with molecular processes (e.g., adsorption, diffusion, reaction), multiscale approaches that combine wave function theory, periodic density functional theory and classical force fields are often necessary [8]. While a number of broadly-applicable software packages are available for performing these calculations [10], a software toolkit for zeolite-specific tasks would be valuable. In this work, we describe the design and capabilities of a new python-based open-source software package — Multiscale Atomistic Zeolite Simulation Environment (MAZE).

The increasing availability of open-source software packages [11] that offer an user-friendly interfaces has greatly simplified the process of performing computational chemistry calculations.

For example, the Atomic Simulation Environment (ASE), provides interfaces to various computational chemistry codes (e.g., VASP [12], LAMMPS [13], GPAW [14]). ASE provides Python-based wrappers to the underlying quantum chemical simulation code and offers an intuitive application programming interface (API) for setting up, starting, and analyzing calculations [15,16]. By automating the cumbersome computational setups and subsequent data analysis, ASE simplifies the process of performing and analyzing complex calculations [15,17]. Furthermore, by allowing manipulation through Python scripts, rather than a GUI, these calculations become self-documenting, reproducible and easy to streamline into complex workflows [11,15].

Problems and background

Current limitations with tracking atoms within the ASE interface

Despite an active user community and continued developments within the ASE codebase [15], a few specific structural manipulation tasks are challenging to implement within ASE. Often a variety of structural manipulations (e.g., extracting and reinserting clusters, adding terminal H atoms etc.) are necessary to address a zeolite-specific scientific question—the current ASE interface is not well suited for ‘‘tracking’’ the resulting changes in the atom indices. This is illustrated using a simple example below.

In ASE, groups of atoms are represented in memory by Atoms Python objects. In an Atoms object, the properties of all of the atoms are stored in NumPy arrays. When a specific atom in an Atoms object is accessed using the get_item method (e.g., my_atoms[index]) an Atom object is

created, which has (among others) the attributes ‘tag’, ‘position’, ‘symbol’ and ‘index’. The underlying data structure for storing the atoms properties is highly efficient, since it does not require storing an individual Python object for each atom represented by an Atoms object. Unfortunately, it also means that the indices of each atom can change with each addition or deletion. Fig. 1 shows the structures and atom indices for various glyoxal derivatives, demonstrating how structural manipulations can alter the indices of atoms.

Structure	Transformation	Indices of the NumPy Array							
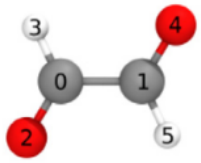	None	0	1	2	3	4	5	None	None
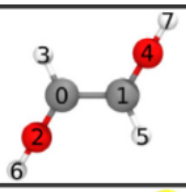	Add Two H Atoms	0	1	2	3	4	5	6	7
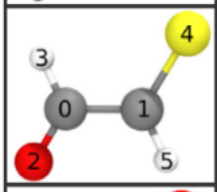	Replace the O Atom by S	0	1	2	3	4	5	None	None
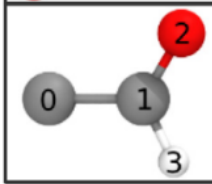	Delete the O and H on C1	0	1	None	None	2	3	None	None

Fig. 1. Relationship between indices in Atoms objects derived from glyoxal. The columns relate the indices of different Atoms objects to each other and the atoms in each structure are labeled with their corresponding indices.

The indices shifting issue becomes more pronounced when multiple structural operations are performed in series. For example, if the O and H atoms are added back to #3 to recover #1, their indices (4 and 5) would differ from the initial structure

Fig. 1 shows how the indices of the individual atoms can change when additions and deletions are performed. The most pronounced difference is in the fourth structure, where the deletion of two atoms causes the decrement of the index 4 and 5 to 2 and 3 respectively. The addition of atoms simply extends the arrays and are thus added to the end. There is no inherent ordering in the indices; the order in which atoms are added to a structure effects the final order of atoms. If a substitution is made by changing the identity of a given atom, then the indices remain unchanged. The mutability of Atoms objects, and subsequent index shifting, introduces significant complexity in tracking the relationship and identity of atoms. These are a major bottlenecks for developing workflows that include both periodic and cluster calculations with zeolites.

Fig. 2. Simplified unified modeling language (UML) class diagram for the Zeolite object. Inheritance relationships are denoted by an open arrow. The Zeolite class inherits from the PerfectZeolite class, which inherits from the Atoms class.

The MAZE solution

Recognizing the challenges outlined above, the MAZE package puts the atom relationship tracking at the center of its design, while maintaining compatibility with all existing ASE's features. As demonstrated in the following sections, it greatly simplifies zeolite workflows and reduces the difficulty in performing a series of structural manipulations.

MAZE architecture

Architecture overview

The MAZE project aims to include all of the functionality of the base ASE package while including additional functionality related to the tracking of atoms. This is incorporated by using inheritance. A zeolite is a group of atoms, so it is appropriate to create a Zeolite class that inherits from ASE's Atoms class. The Zeolite class represents a zeolite and includes additional methods and properties for identifying the unique crystallographic sites. Polymorphism ensures that the Zeolite class has all of the attributes and methods of the parent Atoms class. Thus, all of ASE's methods and classes also work well with it.

The additional functionality of the Zeolite class is divided between two classes, the parent PerfectZeolite class and its sub-class Zeolite. The PerfectZeolite class includes the functionality for building a Zeolite from a labeled CIF file and preserving the site labels. The methods included in the PerfectZeolite are all of those related to site identification, and serialization. In a group of zeolites there can be only one perfect zeolite, from which all the derivatives (e.g.,

Bronsted H versions, adsorbates etc.) are made. A simplified unified modeling language (UML) class diagram for the Zeolite and PerfectZeolite classes is presented in Fig. 2.

Users of the MAZE package will interact primarily with Zeolite objects. The main additional features of the Zeolite class versus the PerfectZeolite class are related to atom manipulation, such as adding atoms, deleting atoms, extracting clusters and capping clusters. By dividing the functionality between two classes, the attributes that make a Zeolite and those involved in structural manipulation can be separated, greatly simplifying the underlying code. The underpinning of the Zeolite functionality is an internal IndexMapper object, which tracks the relationship between the indices of the atoms in the zeolites derived from the same parent structure.

The IndexMapper class

The instances of the IndexMapper class are responsible for tracking the relationship between atom indices. A reference to an IndexMapper object is an attribute of each Zeolite class and related Zeolites share the same IndexMapper. The IndexMapper does not directly encounter Atoms objects, but only works with their indices. The core data structure of the IndexMapper is the main_index, which consists of a collection of nested dictionaries. The key of the outer dictionary is the unique id of each row of atoms in the object (Fig. 3). The inner dictionary consists of each zeolites name attribute followed by the index of an Atom or a None object.

```
{0: {"parent": 0, "Zeolite_1": 0, "Cluster_3": None, "Open Defect_5": 0},
 1: {"parent": 1, "Zeolite_1": 1, "Cluster_3": None, "Open Defect_5": 1},
 2: {"parent": 2, "Zeolite_1": 2, "Cluster_3": 0, "Open Defect_5": None},
 3: {"parent": 3, "Zeolite_1": 3, "Cluster_3": None, "Open Defect_5": 2},
 4: {"parent": 4, "Zeolite_1": 4, "Cluster_3": None, "Open Defect_5": 3},
 # ...
 188: {"parent": 188, "Zeolite_1": 188, "Cluster_3": None, "Open Defect_5": 167},
 189: {"parent": 189, "Zeolite_1": 189, "Cluster_3": None, "Open Defect_5": 168},
 190: {"parent": 190, "Zeolite_1": 190, "Cluster_3": None, "Open Defect_5": 169},
 191: {"parent": 191, "Zeolite_1": 191, "Cluster_3": None, "Open Defect_5": 170}}
```

Fig 3. Dictionary representation of the main index mapper for a collection of related Zeolites. The keys of the outer dictionary represent the unique IDs, where the inner dictionaries map the relationship between indices for the same shared atom across different Atoms-like objects

The main_index in the IndexMapper object records the relationship indices of different Atoms objects. The unique_id assigns a unique identifier (ID) to each atom. This ID does not depend on the atom species and if an atoms type is changed from silicon to tin, for example, the ID remains unchanged. The row shows the relationship between the indices across different Atoms objects. For example, in row four (i.e., index 3 of the dictionary), the ID equals 3 and the indices of the parent, Zeolite_1 and Open Defect_5 are all equal to 3. The equivalent atom index in Cluster_3, which consists of an extracted cluster from Zeolite_1 is 0. Cluster_3 consists of 21 atoms, and the Open Defect_5 object consists of all of the atoms in Zeolite_1 with the exception of the atoms in Cluster_3. Thus, Open Defect_5 final indices are offset by 21 as can be seen in the final rows of the table.

The main_index is automatically updated when each atom manipulation operation is performed and does not require additional intervention from the user. The index mapper class can be used to

directly map between two related zeolites with the get_index function, yet its core benefit comes about by enabling the structural manipulation functions such as cap_atoms and Integrate.

Complimenting this index mapper are the add_atoms and delete_atoms methods in the Zeolite class, which return a copy of the original Zeolite object with the applied modifications and append a new column to the IndexMapper's main index. This new column contains the indices of the newly created Zeolite object and each row indicates the relationship between the atoms in other zeolites. If a Zeolite object is deleted, then the deconstructor will remove its corresponding entry from the IndexMapper, preventing the main index from being cluttered with deleted Zeolite object indices.

Illustrative examples

To demonstrate the capability of the MAZE code and assess its API three distinct tasks were performed. These tasks include building a Zeolite object from a labeled International Zeolite Association (IZA) CIF file, adding and removing atoms, and a complete workflow involving removing a cluster, changing some of its atoms and reinserting it back into the original zeolite.

Building a zeolite from a CIF file

Zeolites often contain multiple distinct T-sites, each of which has unique chemistries arising from differences in the local atomic environment. Comprehensive zeolite screenings studies require all unique T sites to be systematically explored. Computational studies of this type start by downloading a CIF file from the IZA database, placing the file in the project folder and reading the CIF file into an Atoms object with the ase.io.read function. One challenge with this approach

is that CIF files downloaded from the IZA database contain extra information about the identity of unique atoms, which is not preserved when the CIF file is loaded with ASE's read function. Thus, various ''hacks'' are needed to align the Atoms object built from the CIF file with their labels. One hack used in our group involves changing a unique site from a silicon to an unused atom such as xenon, and when the Atoms object is loaded reverting it back to a silicon, noting the indices (see Fig. 4, right). This manual tagging mechanism is slow, opaque because the code is no longer self-documenting, and error prone, since it involves manually editing a critical data file.

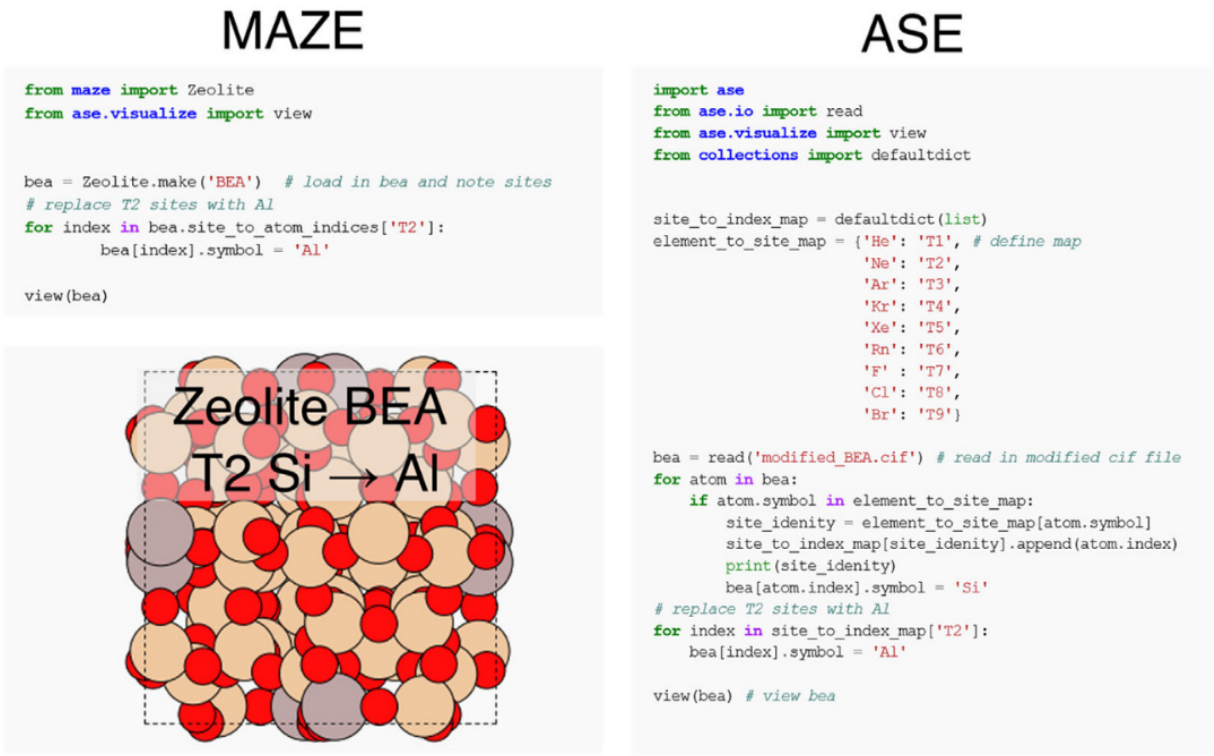

Fig. 4. Comparison between MAZE and ASE code for generating a BEA zeolite structure with the Silicon T2 sites replaced by aluminum atoms. The MAZE code uses the built-in make function to read the unmodified CIF file and

store the mapping in the site_to_atom_indices dictionary. The longer ASE code requires a modified CIF file as input, and the element mapping to be manually defined. Both codes generate and visualize the same BEA T2 Si→Al structure.

The MAZE package significantly improves this process by introducing the make method. The make method takes a zeolite IZA code as input, looks for the corresponding CIF file, and if it is not found attempts to download the zeolite CIF file from the IZA database. After locating or downloading the correct CIF file, the make function then builds a Zeolite from a IZA CIF file, and stores the mapping between the indices and their identities in two of the Zeolite objects internal dictionaries. The identities of the sites can then be determined by using the get_site_type method or by accessing the dictionaries directly (Fig. 4).

Structural manipulations

The Atoms class' structural manipulation features allow atoms to be added and removed from the collection and the properties of individual atoms to be altered. The API by which these manipulations are performed is inspired by Python's list manipulation methods. Although familiar to Python users, these manipulations are not self-consistent as some have side effects (e.g., the pop method) while others are side effect free such as the __add__ method. In zeolite workflows, it is common for many derivatives of a single parent zeolite to be generated, and this is complicated by methods with side-effects, due to the need for explicit copying prior to each modification.

In alignment with the goal of the MAZE project, new methods for atomic manipulation were designed, which do not mutate the underlying object, and instead return a copy with the applied

modifications. These methods (add_atoms and delete_atoms) simplify the computational workflows and also allow for method chaining improving code readability. A list of the available methods for the ASE Atoms object and the MAZE Zeolite object are shown in table S1.

Cluster extraction, atom capping and integration

The power of these additional structural manipulation features can be demonstrated by performing a complex workflow. A typical zeolite unit cell contains over one-hundred atoms, but the region of chemical interest is frequently confined to the atoms adjacent to a few T-sites. To reduce the computational expense of quantum chemical calculations, the calculations are typically performed on a smaller subset of atoms adjacent to the active sites of interest. This subset of atoms is referred to as a cluster [18]. Capping atoms (usually, hydrogens) are added to the terminal cluster atoms to make chemically meaningful structures. The optimal position for the capping atoms is based on the parent zeotype's structure. After the capped cluster's structure has been optimized, the cluster can be integrated back into the initial zeolite for further downstream analysis.

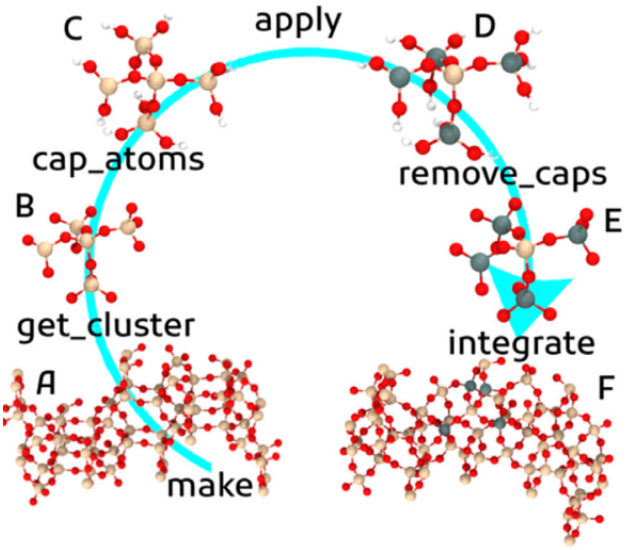

Fig. 5. Workflow for cluster integration. A blue arrow shows the workflow direction, starting with a BEA zeolite constructed using the make method. The functions or operations required to transfer from one structure to another are shown between the structures on the blue line.

This workflow is extraordinarily difficult to perform with the ASE base package due to the challenge associated with tracking the relationship between atom indices during the extraction, manipulation, and reinsertion step. The Zeolite class's built-in index mapper ensures that the relationship between atoms can easily be determined and forms the basis for the simple functions that perform this workflow. In Fig. 5 a pictorial representation of stages in the workflow is shown along with the methods needed to perform the transformation from one stage to the next. The overall workflow has six distinct structures bridged by functions which take the previous structure as an input and output the new structure. The cluster structures (B, C, D, E) have different indices than the BEA frameworks (A, F), yet the indices can easily be mapped to each other using the built-in IndexMapper's get_index method. Since the functions do not alter the zeolite to which they are applied, and instead return a new zeolite object, they can be chained

together. The chained methods required to transform structure A into structure F is shown in Fig. 6.

```
from maze import Zeolite
def change_atoms(atoms):
    for atom in atoms:
        if atom.symbol == 'Si' and atom.tag != 154:
            atoms[atom.index].symbol = 'Sn'

bea = Zeolite.make('BEA')
cluster = bea.get_cluster(154)[0].cap_atoms().apply(change_atoms).remove_caps()
bea_sn = bea.integrate(cluster)
```

Fig. 6. Code required to generate structure F from structure A.

The code presented in Fig. 6 demonstrates how a complex workflow can be achieved with the chaining of several functions together. This simplicity allows for knowability of the operations, precise and complete operability, and robustness due to high readability. The scrambling of the indices with the cluster extraction does not allow for consistent code using the base ASE package. Instead, the indices of each atom must be matched manually at each stage of the process. Thus, the MAZE package interface has increased the knowability, operability and robustness compared to the cumbersome manual workflow required when using the base ASE package.

Impact and conclusion

The improved API of the MAZE package was presented here by demonstrating how to perform representative tasks. Several other features of the MAZE package include database integration and adsorbate additions. A complete description can be found in the documentation, which is

referenced in the supplementary material. MAZE's improved API builds on-top of the Atomic Simulation Environment. This new interface facilitates computational zeolite calculations by greatly simplifying the steps needed to perform common zeolite tasks. [2] Computational experiments are less labor intensive than wet lab experiments, but lack of optimal APIs for scientific software and complex workflows can incur a significant time commitment from researchers to setup and run. By creating custom software tailored to the specific task, research can be simplified and larger scale experiments can be conducted.

References

(1) Smit B, Maesen TLM. Towards a molecular understanding of shape selectivity. Nature 2008;451(7179):671–8. http://dx.doi.org/10.1038/nature06552.

(2) Xie P, et al. Bridging adsorption analytics and catalytic kinetics for metal-exchanged zeolites. Nat Catal 2021;4(2):144–56. http://dx.doi.org/10.1038/s41929-020-00555-0.

(3) Kosinov N, Liu C, Hensen EJM, Pidko EA. Engineering of transition metal catalysts confined in zeolites. Chem Mater 2018;30(10):3177–98. http://dx.doi.org/10.1021/acs.chemmater.8b01311.

(4) Mohan S, Dinesha P, Kumar S. NOx reduction behaviour in copper zeolite catalysts for ammonia SCR systems: A review. Chem Eng J 2020;384:123253. http://dx.doi.org/10.1016/j.cej.2019.123253.

(5) Sushkevich VL, van Bokhoven JA. Methane-to-methanol: Activity descriptors in copper-exchanged zeolites for the rational design of materials. ACS Catal 2019;9(7):6293–304. http://dx.doi.org/10.1021/acscatal.9b01534.

(6) Astala R, Auerbach SM, Monson PA. Density functional theory study of silica zeolite structures: Stabilities and mechanical properties of SOD, LTA, CHA, MOR, and MFI. J Phys Chem B 2004;108(26):9208–15. http://dx.doi.org/10.1021/jp0493733.

(7) Zheng X, Blowers P. A computational study of methane catalytic reactions on zeolites. J Mol Catal A: Chemical 2006;246(1–2):1–10. http://dx.doi.org/10.1016/j.molcata.2005.10.009.

(8) Catlow CRA, Van Speybroeck V, van Santen R. Modelling and Simulation in the Science of Micro- and Meso-Porous Materials. Saint Louis, UNITED STATES; 2017, [Online]. Available http://ebookcentral.proquest.com/lib/ucdavis/detail.action?docID=5051428.

(9) Weckhuysen BM, Yu J. Recent advances in zeolite chemistry and catalysis. Chem Soc Rev 2015;44(20):7022–4. http://dx.doi.org/10.1039/C5CS90100F.

(10) Himanen L, Geurts A, Foster AS, Rinke P. Data-driven materials science: Status, challenges, and perspectives. Adv Sci 2019;6(21):1900808. http://dx.doi.org/10.1002/advs.201900808.

(11) Pirhadi S, Sunseri J, Koes DR. Open source molecular modeling. J Mol Graph Model 2016;69:127–43. http://dx.doi.org/10.1016/j.jmgm.2016.07.008.

(12) Kresse G, Joubert D. From ultrasoft pseudopotentials to the projector augmented-wave method. Phys Rev B 1999;59(3):1758–75. http://dx.doi.org/10.1103/PhysRevB.59.1758.

(13) Plimpton S. Fast parallel algorithms for short-range molecular dynamics. J Comput Phys 1995;117(1):1–19. http://dx.doi.org/10.1006/jcph.1995.1039.

(14) Mortensen JJ, Hansen LB, Jacobsen KW. Real-space grid implementation of the projector augmented wave method. Phys Rev B 2005;71(3):035109. http://dx.doi.org/10.1103/PhysRevB.71.035109.

(15) Hjorth Larsen A, et al. The atomic simulation environment—a Python library for working with atoms. J Phys: Condens Matter 2017;29(27):273002. http://dx.doi.org/10.1088/1361-648X/aa680e.

(16) Mosqueira-Rey E, Alonso-Ríos D, Moret-Bonillo V, Fernández-Varela I, Álvarez-Estévez D. A systematic approach to API usability: Taxonomy-derived criteria and a case study. Inf Softw Technol 2018;97:46–63. http://dx.doi.org/10.1016/j.infsof.2017.12.010.

(17) Bahn SR, Jacobsen KW. An object-oriented scripting interface to a legacy electronic structure code. Comput Sci Eng 2002;4(3):56–66. http://dx.doi.org/10.1109/5992.998641.

(18) Schroeder C, et al. A stable silanol triad in the zeolite catalyst SSZ-70. Angew Chem Int Ed 2020;59(27):10939–43. http://dx.doi.org/10.1002/anie. 202001364.

Chapter 2

Elucidating Cooperative Interactions between Grafted Amines and Tin or Titanium Sites on Silica

Christine Khoury, Samuel Holton, Dina Shpasser, Elior Hallo, Ambarish Kulkarni, Friederike C. Jentoft, and Oz M. Gazit

Adapted with permission from ACS Catal. 2022, 12, 9846−9856.

I provided the theory sections of this paper. Some paper sections have been removed to emphasize theory contributions, with original figure numbers retained.

Abstract

The efficient promotion of cooperative catalytic interactions on solid surfaces can be of great benefit for a range of important reactions. Herein, we demonstrate that the cooperative interactions of isolated tin (Sn) and titanium (Ti) sites on silica with grafted primary amines (NH2) can be tuned by changing the immediate chemical environment of the metal sites (M). We show that, by tethering various size organic ligands (RO) to the M sites, we can govern the interactions between the sites as measured by the

presence of NH3+. We show that the concentration of NH3+ is directly correlated with the activity of the model Henry reaction. We further find that the selectivity to the olefinic product increased from 59% for the cooperative interactions of grafted NH2 and surface silanols to

84–92% for the cooperative interactions between grafted NH2 and the isolated Sn or Ti sites. An analysis by DFT shows that these cooperative interactions are enabled by the presence of a trace amount (two molecules per M site) of water near the metal sites and a resulting hydrolysis, which depends on the hydrophobicity of the RO group and the nature of the metal. Hence, the current work provides advanced molecular-level insights into the underlying principles of cooperative interactions on a solid surface and guidance for governing such interactions by tuning the chemical environment.

Introduction

Cooperative heterogeneous catalysts are a class of materials that contain at least two active sites that work in concert to activate an electrophile and a nucleophile to promote a single chemical transformation [1] The cooperative mechanism is accompanied by a lower activation energy, which allows conducting the reaction under milder conditions as well as increases the overall catalyst activity and may also lead to a higher selectivity, in comparison with single-site catalyst analogues [2] As such, this class of heterogeneous catalysts can make the overall chemical process significantly more environmentally friendly. However, inducing and even more so controlling the cooperative catalytic interactions on a solid material is a challenging task [1,3–5]. To synthesize an efficient cooperative catalytic material, three architectural levels in material design need to be engineered: (1) the 3D structure of the support, (2) the immediate chemical environment surrounding the catalytic site, and (3) the precise positioning and orientation of the catalytic sites [3].

Materials involving amine sites grafted on amorphous silica have been extensively demonstrated to promote cooperative catalytic interactions for reactions such as the aldol condensation and others [6–17]. The liquid-phase aldol condensation and nitroaldol condensation are an important class of reactions in green chemistry and enable the conversion of biomass-derived molecules to fuels and chemicals [18] Specifically, the Henry reaction (see Figure 1) has been extensively used in the literature as a probe reaction to monitor changes in the level of cooperative interactions between grafted NH2 and surface silanols [15,16,19]. Mechanistically, it has been shown that the direct formation of the unsaturated product via the imine route is due to cooperative interactions between the NH2 and surface silanol sites [16]. Therefore, the selectivity of the Henry reaction toward the unsaturated (olefinic) product serves as a descriptor for identifying cooperative interactions between the acid and base functions.

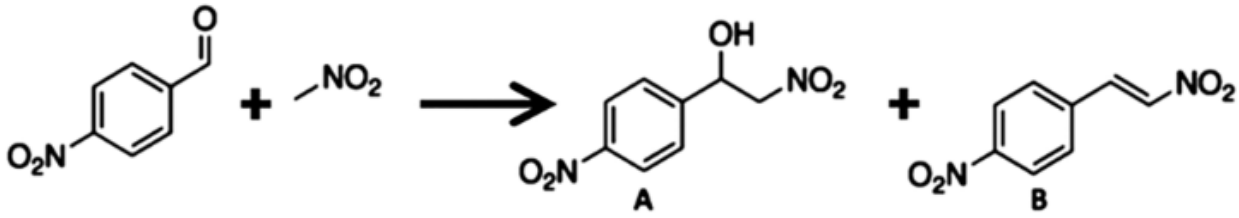

Figure 1. Henry reaction of 4-nitrobenzaldehyde and nitromethane forming the alcoholic product (A) and unsaturated (olefinic) product (B).

Studies of cooperative interactions between silanols on amorphous silica and grafted NH2 allowed the isolation of structural and chemical parameters affecting the cooperative interactions. Specifically, the effect of proximity and orientation between the OH and NH2 on the surface [20], acid to base ratio (OH:NH2) [19], silica porosity [19], and the immediate chemical

environment surrounding the base site have all been rigorously evaluated [16]. However, because of its amorphous nature, silica is inherently nonuniform, leading to a nonrandom spatial distribution of grafted amines, which in turn leads to amine clustering and pore blockage [21]. In addition, the rigid structure of silica restricts active site configurational movement, which has been shown to be important with respect to the efficiency of catalytic cooperativity [20]. The consequence of these limitations is evident in the separate works of both Moschetta et al. and Bass et al. In both works a maximum of ~80% selectivity to the olefinic product of the Henry reaction of 4-nitrobenzaldehyde and nitromethane is reached using grafted propyl amines on silica as the catalyst [13, 16].

With the aim of improving the efficiency and control of cooperative interactions on solid surfaces, herein we examine the performance of isolated tin (Sn) and titanium (Ti) sites grafted separately on aminopropyl-functionalized silica. These metals were specifically chosen as they have been shown to function cooperatively with primary amine sites on the backbone of chitosan [22, 23]. As previously reported for such metals, the hybrid coordination environment comprised of organic and inorganic ligands renders a material with improved hydrolytic and mechanical stability [4]. Specifically, grafted Ti and Sn sites on silica type materials have been demonstrated to be reactive and stable for a range of reactions [24, 27]. By a combined experimental and computational analysis, we show that the Sn and Ti sites both cooperatively catalyze the reaction more efficiently in comparison to amine-functionalized SiO2 but only in the presence of a trace amount of water. We further show that the catalytic activity can be governed by manipulating the chemical environment, which is dictated by the size of a grafted alkoxy group.

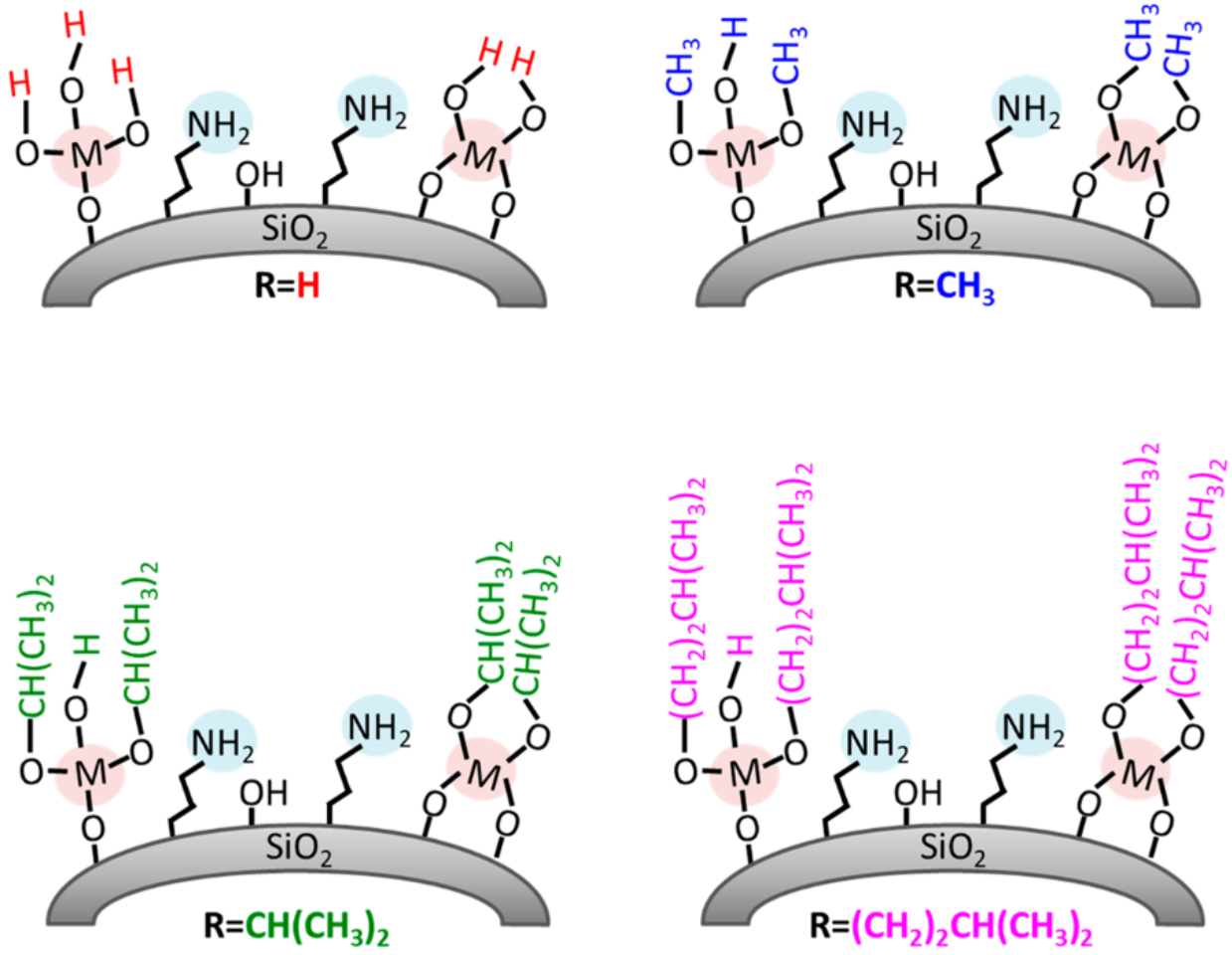

Figure 2. Schematic representation of the various RO-M/APS materials. The M represents an Sn or Ti site. The grafting of the –OR groups was accomplished by the initial grafting of either SnCl4 or TiCl4 to react with Si–OH on the surface of APS and removal of the excess precursor

followed by the introduction of the –OR group (see the Supporting Information for detailed experimental information).

Computational analysis

A β-cristoballite surface (obtained from the IZA database) is used as a representative model of the amorphous silica support owing to its similar silanol density [62]. The siliceous structure and unit cell parameters are optimized using the PBE functional in Vienna Ab Initio Simulation Package (VASP) with an energy cutoff of 500 eV and D3BJ dispersion correction. The optimized

unit cell is used to construct a large cluster model (50 Si, capped with terminal H atoms, H atom positions are optimized) and is placed in a large simulation cell. Similar to other slab models, the bottom 2 layers of the structure are constrained and are held fixed during the optimization. The necessary organic groups (e.g., 3-aminopropanol and the metal complex) are added to the surface and are optimized at the energy cutoff of 500 eV until the forces are less than 0.05 eV/Å. All DFT calculations are performed using the Γ point. Similar procedure is used for the Sn and the Ti moieties.

Results and Discussion

Briefly, the catalytic materials were prepared by grafting a metal (M) acid site of Sn or Ti on commercially available aminopropyl-functionalized silica (APS) using tetrachloride precursors (see the Supporting Information for full synthesis details). Notably, to avoid variations in the average amine surface concentration and distribution, the same batch was used for all grafted materials. The Sn or Ti sites were subsequently grafted with OH groups or alkoxy groups of different molecular sizes through the exchange of the Cl ligand with an RO ligand. These obtained materials are denoted as RO-M/APS, where M = Sn/Ti and R = H, CH3, CH(CH3)2, (CH2)2CH(CH3)2 (see Figure 2).

All materials were characterized using powder X-ray diffraction (PXRD), N2 physisorption, diffuse reflectance UV−vis spectroscopy, diffusive reflectance infrared Fourier transform spectroscopy (DRIFTS), and X-ray photoelectron spectroscopy (XPS). The results for material characterization were cross-referenced with kinetic measurements for the Henry reaction.

Analyzing the samples using XPS allowed quantification of the extent of interaction between M−OH and adjacent NH2 sites. The core level spectra for all the RO-Sn/APS and RO-Ti/APS materials were recorded for C 1s, O 1s, and N 1s (Figure 6) and for Sn 3d and Ti 2p (Figure S2). The O 1s spectra of all the RO-Sn/APS materials showed the formation of a peak at 531.9 ± 0.2 eV attributed to Sn−O−C and Sn−OH bonds following grafting (Figure 6) [50,51]. In all samples the O 1s peak at 531 ± 0.1 eV corresponds to the silane Si−O bond of the grafted aminopropyl silane.52 The O 1s spectra of the RO-Ti/APS materials showed the formation of two peaks at 530.0 ± 0.1 and 531.9 ± 0.1 eV corresponding to Ti−O−C and Ti−OH bonds, respectively [53]. The grafting of the M sites to the silica surface was accompanied by a decrease in the peak area at 533.6 ± 0.2 eV attributed to the Si−OH bond [54], showing that the grafting occurred through the silica surface hydroxy groups. This gives us the ability to calculate for each sample the ratio between the amount of M−O−R bonds formed and the number of Si−OH groups reacted (Table 2). It can be seen that for all samples the M−O−Rformed/Si−OH reacted ratio was greater than 1, which indicates that the number of −OR groups is equal to or greater than the number of M−O−Si bonds. For a tetrahedral configuration, the ratio suggests that the M sites are grafted in a monodentate (Si−O−M−(O−R)3) or bidentate ((Si−O)2−M−(O−R)2) configuration, which is typical for room-temperature grafting [55] Interestingly, the M−O−Rformed/Si−OH reacted ratio was found to be specific for the type of RO group tethered to the M site. Hence, it can be assumed that each of the R−OH molecules has a specific affinity to the Cl−M site.

From the O 1s XP spectra of the RO-Ti/APS materials it was found that the Ti−OH/Ti−O−C ratios for the CH3O-Ti/APS, CH(CH3)2O-Ti/APS and (CH2)2CH(CH3)2O-Ti/APS materials were 2.2 ± 0.4, 1.5 ± 0.3, and 3.3 ± 0.7, respectively. This clearly shows that each Ti site is

coordinated to at least one OR ligand. The remaining M−Cl sites formed Ti−OH, most likely due to a reaction with trace water in the grafting solution. The same analysis could not be done for the Sn system, as the O 1s peaks of Sn−O and Sn−OR overlap completely.

The N 1s signal of the native APS material shows a peak at 399.15 ± 0.2 eV corresponding to the existence of only NH2 species, which was typically reported to appear at 399.3−399.5eV [56, 57]. Upon M grafting, a new peak appears at (401.4−401.6) ± 0.2 eV, which is attributed to the formation of protonated NH3+ (Figure 6) [56, 58]. The formation of NH3+ species following M grafting is consistent with the DRIFTS results above and accounts for 20−45% of the total amine present in the samples. Notably, in the presence of excess triethylamine the metal chlorides may also react to form a Sn/Ti−amide bond [57]. Farfan-Arribas et al. reported the appearance of a 401.1 eV band related to a Ti−amide bond following the adsorption of dimethyl amine on TiO2.59 Head et al. attributed binding energies of 398.6 and 400.3 eV to the presence of Ti−amide bonds in neutral and protonated forms, respectively [60]. These observations and our own show that the N 1s peak is significantly dependent on the chemical environment. Although we cannot rule out the formation of a metal−amide bond, on the basis of the DRIFTS data discussed above, we relate the higher-binding-energy XP peak here to amine protonation by the interaction of the amine with an adjacent species. Moreover, the grafting procedure is conducted in the presence of triethylamine, which scavenges free HCl in solution, thus suppressing formation of NH3+ species through amine protonation by HCl [23].

On the basis of the XPS atomic concentration percent (AC percent) we find that in all the grafted samples the atomic percent of N in the NH3+ form is greater than the atomic percent of residual

Cl (Table 3), which originates from a partially substituted M site. On the assumption that each residual Cl atom accounts for the formation of one NH3+, the percent excess of NH3+ species, exceeding the amount of residual Cl, can be calculated to be 9–33% for the Sn system and 4–34% for the Ti system (Table 3).

Table 2. Calculated Surface Atomic Concentrations (AC) of O, M−O−R_{formed}/Si−$OH_{reacted}$ Ratios on the RO-M/APS Catalyst Surface, and Ti−O−C/Ti−OH Ratios on the RO-Ti/APS Catalyst Surface, from XPS Analysis

	O AC (%)	M−O−R_{formed}/Si−$OH_{reacted}$ [a]	Ti−OH/Ti−O−C
APS	55 ± 1		
HO-Sn/APS	57 ± 1	1.4 ± 0.3	
CH_3O-Sn/APS	55 ± 1	1.3 ± 0.3	
$CH(CH_3)_2O$-Sn/APS	55 ± 1	2.3 ± 0.5	
$(CH_2)_2CH(CH_3)_2O$-Sn/APS	55 ± 1	2.0 ± 0.4	
HO-Ti/APS	57 ± 2	2.0 ± 0.4	
CH_3O-Ti/APS	56 ± 1	3.3 ± 0.7	2.2 ± 0.4
$CH(CH_3)_2O$-Ti/APS	54 ± 1	2.3 ± 0.5	1.5 ± 0.3
$(CH_2)_2CH(CH_3)_2O$-Ti/APS	54 ± 1	1.6 ± 0.3	3.3 ± 0.7

[a]The M−O−R_{formed}/Si−$OH_{reacted}$ and Ti−OH/Ti−O−C ratios were calculated from the area percents of the M−O−R, Si−OH, Ti−OH and Ti−O−C peaks obtained from the deconvolution of the high-resolution O 1s XP spectra. The error in AC based on XPS instrument parameters is 20%.

Table 3. Calculated Surface Atomic Concentrations (AC) of N, Cl, N in NH_3^+ form, and excess NH_3^+ on the RO-M/APS Catalyst Surface, from XPS Analysis

	N AC (%)	Cl AC (%)	AC of N in NH_3^+ form (%)	excess NH_3^+ (%)[a]	AC of Ti−OH (%)
APS	3.0 ± 0.5				
HO-Sn/APS	2.7 ± 0.5	0.30 ± 0.06	1.2 ± 0.2	33 ± 9	
CH_3O-Sn/APS	2.5 ± 0.5	0.42 ± 0.08	1.0 ± 0.2	23 ± 6	
$CH(CH_3)_2O$-Sn/APS	2.3 ± 0.5	0.6 ± 0.1	0.9 ± 0.2	13 ± 3	
$(CH_2)_2CH(CH_3)_2O$-Sn/APS	2.3 ± 0.5	0.5 ± 0.1	0.7 ± 0.1	9 ± 2	
HO-Ti/APS	2.7 ± 0.5	0.28 ± 0.06	1.2 ± 0.2	34 ± 9	0.8 ± 0.2
CH_3O-Ti/APS	2.7 ± 0.5	0.5 ± 0.1	1.2 ± 0.2	25 ± 7	0.8 ± 0.2
$CH(CH_3)_2O$-Ti/APS	2.7 ± 0.5	0.7 ± 0.1	1.1 ± 0.2	15 ± 4	0.9 ± 0.2
$(CH_2)_2CH(CH_3)_2O$-Ti/APS	2.4 ± 0.5	0.5 ± 0.1	0.6 ± 0.1	4 ± 1	0.8 ± 0.2

[a]The AC percent of NH_3^+ for each sample was calculated from the area percent of the NH_2 and NH_3^+ peaks obtained from the deconvolution of the high-resolution N 1s XP spectra. The error in AC based on XPS instrument parameters is ±20%.

We used density functional theory (DFT) calculations to rationalize the excess NH3+ species (see computational details) discussed above. Specifically, our calculations showed that the isolated OH group on the metal (e.g., (OSi)X−Sn−OH) is unlikely to transfer a proton to the amine group. For example, the formation of the −O−Sn−(OCH3)2 state was unstable, and the structure reverted back to an uncharged state. However, when two water molecules were added to the metal to form a stable octahedral complex, the proton readily transferred from a water

molecule to the amine group, forming an ammonium cation and leaving an OH– ligand on the metal, which correlates well with previous work studying amines on silica surfaces. For example, Mafra et al. demonstrated that the presence of a water molecule is required to stabilize a charged carbamic acid like species [61]. Figure 7a,b shows that the charge-separated state is stabilized by a strong electrostatic interaction between the proton and the Sn complex. The electronic energies of the intermediates show that forming a charged complex is energetically favorable for both Sn and Ti. As can be seen in Figure 7c, Sn more readily adsorbs water and participates in charge transfer in comparison to Ti.

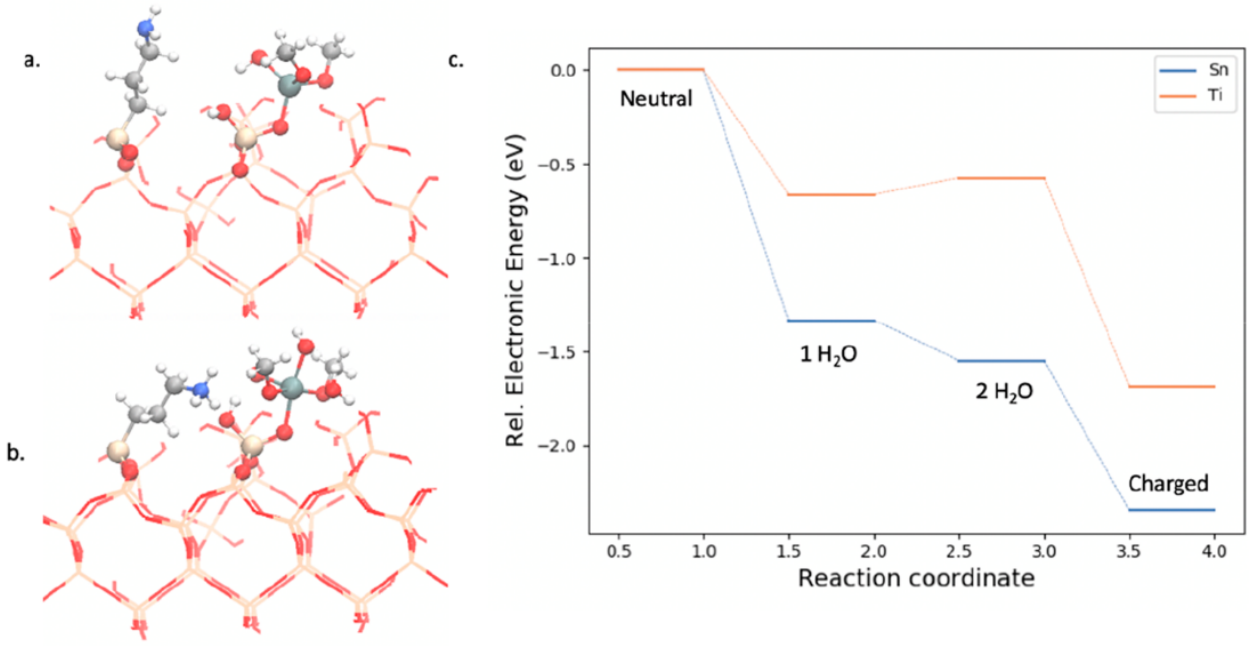

Figure 7. DFT analysis of materials: (a) initial state with a four-coordinate Sn complex; (b) hexacoordinate Sn complex with an OH– ligand and charged amine in close proximity; (c) the relative electronic energies moving from a four-coordinate metal to the final charged complex. Atom legend: red = oxygen, yellow = silicon, gray = carbon, blue = nitrogen, white = hydrogen.

Since the presence of a protic solvent is necessary to facilitate charge transfer between the metal and the amine, this suggests that longer hydrocarbon chains on the metal would exclude protic solvent and result in a more nonpolar environment near the surface. Both of these factors would reduce the population of a charged complex near the surface, which matches the experimental results showing fewer charged complexes in catalysts with longer side chains (Figure 8).

Although the current analysis is limited to the “static” structures, incorporating the flexibility of the organic groups is computationally intensive and is beyond the scope of this study.

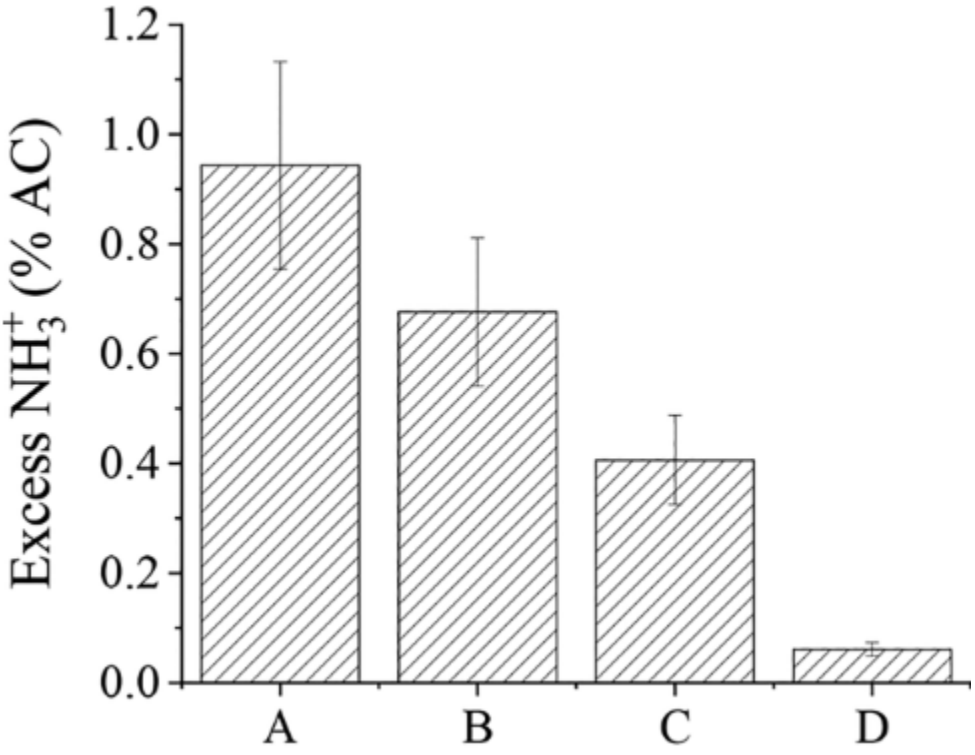

Figure 8. Excess AC percent of NH3+ as a function of the RO group tethered to the Ti site for (A) HO-Ti/APS, (B) CH3O-Ti/APS, (C) CH(CH3)2O-Ti/APS, and (D) (CH2)2CH(CH3)2O-Ti/APS.

Conclusion

In this work, the surface of amino propyl functionalized silica (APS) was grafted with Ti or Sn as isolated sites followed by tethering of various sizes of RO− groups. Catalytic testing for the Henry reaction showed that the Sn or Ti grafting resulted in a higher activity and significantly higher selectivity of 84−92% to the olefinic product, in comparison to the APS control, which showed only 59% selectivity. It was shown that the grafting of Ti and Sn formed a new active site, composed of the cooperative interaction of the M−OH and an adjacent amine. Computational analysis showed that the cooperative interactions and the formation of the stable excess NH3+ species became possible only in the presence of a trace amount of polar solvent (e.g., two water molecules per M site). The amount of excess NH3+ was shown to be dependent on the size of the alkyl chain. Moreover, it was shown that the shortest RO−M groups (OH−M) were the most active and were 2-fold more active than Si−OH. In conclusion, this work shows that the introduction of a surface heteroatom (Ti or Sn) on silica provides a new avenue for significantly improving the cooperative interactions between grafted amines and surface metal hydroxy groups over the performance of the well-studied APS system. Moreover, it is shown that the catalytic performance can be controlled by tailoring the close chemical environment of the active site.

References

(1) Margelefsky, E. L.; Zeidan, R. K.; Davis, M. E. Cooperative Catalysis by Silica-Supported Organic Functional Groups. Chem. Soc. Rev. 2008, 37 (6), 1118–1126.

(2) Aguila, B.; Sun, Q.; Wang, X.; O'Rourke, E.; Al-Enizi, A. M.; Nafady, A.; Ma, S. Lower Activation Energy for Catalytic Reactions through Host-Guest Cooperation within Metal-Organic Frameworks. Angewandte Chemie - International Edition 2018, 57 (32), 10107–10111.

(3) Khoury, C.; Gadipelly, C.; Pappuru, S.; Shpasser, D.; Gazit, O. M. Progress in the Design of Cooperative Heterogeneous Catalytic Materials for C-C Bond Formation. Adv. Funct. Mater. 2020, 30 (18), 1901385.

(4) Diaz, U.; Brunel, D.; Corma, A. Catalysis Using Multifunctional Organosiliceous Hybrid Materials. Chem. Soc. Rev. 2013, 42 (9), 4083.

(5) Fernandes, A. E.; Jonas, A. M. Design and Engineering of Multifunctional Silica-Supported Cooperative Catalysts. Catal. Today 2019, 334, 173–186.

(6) Shylesh, S.; Hanna, D.; Gomes, J.; Krishna, S.; Canlas, C. G.; Head-Gordon, M.; Bell, A. T. Tailoring the Cooperative Acid-Base Effects in Silica-Supported Amine Catalysts: Applications in the Continuous Gas-Phase Self-Condensation of n-Butanal. ChemCatChem. 2014, 6 (5), 1283–1290.

(7) Brunelli, N. A.; Venkatasubbaiah, K.; Jones, C. W. Cooperative Catalysis with Acid-Base Bifunctional Mesoporous Silica: Impact of Grafting and Co-Condensation Synthesis Methods on Material Structure and Catalytic Properties. Chem. Mater. 2012, 24 (13), 2433–2442.

(8) Brunelli, N. A.; Didas, S. A.; Venkatasubbaiah, K.; Jones, C. W. Tuning Cooperativity by Controlling the Linker Length of Silica-Supported Amines in Catalysis and CO 2 Capture. J. Am. Chem. Soc. 2012, 134 (34), 13950−13953.

(9) Xie, J.; Ellebracht, N. C.; Jones, C. W. Inter- and Intramolecular Cooperativity Effects in Alkanolamine-Based Acid-Base Heterogeneous Organocatalysts. ACS Omega 2019, 4 (1), 1110−1117.

(10) He, J.; An, Z.; He, J.; Dai, Y.; Yu, C.; Li, B. Enhanced Heterogeneous Asymmetric Catalysis via the Acid-Base Cooperation between Achiral Silanols of Mesoporous Supports and Immobilized Chiral Amines. J. Catal. 2014, 317, 105−113.

(11) Motokura, K.; Tada, M.; Iwasawa, Y. Cooperative Catalysis of Primary and Tertiary Amines Immobilized on Oxide Surfaces for One-Pot C-C Bond Forming Reactions. Angewandte Chemie -International Edition 2008, 47 (48), 9230−9235.

(12) Motokura, K.; Viswanadham, N.; Dhar, G. M.; Iwasawa, Y. Creation of Acid-Base Bifunctional Catalysis for Efficient C-C Coupling Reactions by Amines Immobilization on SiO2, Silica-Alumina, and Nano-H-ZSM-5. Catal. Today 2009, 141 (1−2), 19−24.

(13) Moschetta, E. G.; Brunelli, N. A.; Jones, C. W. Reaction-Dependent Heteroatom Modification of Acid-Base Catalytic Cooperativity in Aminosilica Materials. Applied Catalysis A: General 2015, 504, 429−439.

(14) Elmekawy, A. A.; Sweeney, J. B.; Brown, D. R. Efficient Synthesis of Supported Proline Catalysts for Asymmetric Aldol Reactions. Catalysis Science and Technology 2015, 5 (2), 690−696. (15) Collier, V. E.; Ellebracht, N. C.; Lindy, G. I.; Moschetta, E. G.; Jones, C. W.

Kinetic and Mechanistic Examination of Acid-Base Bifunctional Aminosilica Catalysts in Aldol and Nitroaldol Condensations. ACS Catal. 2016, 6 (1), 460−468.

(16) Bass, J. D.; Solovyov, A.; Pascall, A. J.; Katz, A. Acid-Base Bifunctional and Dielectric Outer-Sphere Effects in Heterogeneous Catalysis: A Comparative Investigation of Model Primary Amine Catalysts. J. Am. Chem. Soc. 2006, 128 (11), 3737−3747.

(17) Pazdera, J.; Berger, E.; Lercher, J. A.; Jentys, A. Conversion of CO2 to Methanol over Bifunctional Basic-Metallic Catalysts. Catal. Commun. 2021, 159, 106347.

(18) Climent, M. J.; Corma, A.; Iborra, S. Conversion of Biomass Platform Molecules into Fuel Additives and Liquid Hydrocarbon Fuels. Green Chem. 2014, 16 (2), 516−547.

(19) Brunelli, N. A.; Jones, C. W. Tuning Acid-Base Cooperativity to Create next Generation Silica-Supported Organocatalysts. J. Catal. 2013, 308 (0), 60−72.

(20) Brunelli, N. A.; Didas, S. A.; Venkatasubbaiah, K.; Jones, C. W. Tuning Cooperativity by Controlling the Linker Length of Silica-Supported Amines in Catalysis and CO2 Capture. J. Am. Chem. Soc. 2012, 134 (34), 13950−13953.

(21) El Kadib, A. Chitosan as a Sustainable Organocatalyst: A Concise Overview. ChemSusChem 2015, 8 (2), 217−244.

(22) Khoury, C.; Gazit, O. M. Self-Organized Porous Titanium-Chitosan Hybrid Materials with Tunable Functions. ChemNanoMat 2018, 4 (4), 353−360.

(23) Khoury, C.; Pappuru, S.; Gavriely, N.; Kleinerman, O.; Shpasser, D.; Segal-Peretz, T.; Gazit, O. M. Cooperatively Catalyzed Henry Reaction through Directed Metal-Chitosan Interactions. ChemNanoMat 2019, 5 (12), 1498. (24) Notestein, J. M.; Andrini, L. R.; Requejo, F. G.; Katz, A.; Iglesia, E. The Role of Outer-Sphere Surface Acidity in Alkene Epoxidation Catalyzed by Calixarene-Ti(IV) Complexes. J. Am. Chem. Soc. 2007, 129 (50), 15585−15595.

(25) Moliner, M.; Román-Leshkov, Y.; Davis, M. E. Tin-Containing Zeolites Are Highly Active Catalysts for the Isomerization of Glucose in Water. Proc. Natl. Acad. Sci. U. S. A. 2010, 107 (14), 6164–6168.

(26) Conrad, S.; Verel, R.; Hammond, C.; Wolf, P.; Göltl, F.; Hermans, I. Silica-Grafted SnIV Catalysts in Hydrogen-Transfer Reactions. ChemCatChem. 2015, 7 (20), 3270–3278.

(27) Zaldivar, G. A. P.; Gushikem, Y.; Kubota, L. T. Tin(IV) Oxide Grafted on a Silica Gel Surface as a Conducting Substrate Base for Cupric Hexacyanoferrate. Journal of Electroanalytical Chemistry and Interfacial Electrochemistry 1991, 318 (1–2), 247–254.

(28) Musić, S.; Filipović-Vinceković , N.; Sekovanić, L. Precipitation of Amorphous SiO2 Particles and Their Properties. Brazilian Journal of Chemical Engineering 2011, 28 (1), 89–94.

(29) Thommes, M.; Kaneko, K.; Neimark, A. V.; Olivier, J. P.; Rodriguez-Reinoso, F.; Rouquerol, J.; Sing, K. S. W. Physisorption of Gases, with Special Reference to the Evaluation of Surface Area and Pore Size Distribution (IUPAC Technical Report). Pure Appl. Chem. 2015, 87 (9–10), 1051–1069.

(30) Charlot, A.; Cuer, F.; Grandjean, A. The Effect of Pore Diameter in the Arrangement of Chelating Species Grafted onto Silica Surfaces with Application to Uranium Extraction. New J. Chem. 2017, 41 (2), 503–511.

(31) Zhou, W.; Liu, Y.; Yang, Y.; Wu, P. Band Gap Engineering of SnO2 by Epitaxial Strain: Experimental and Theoretical Investigations. J. Phys. Chem. C 2014, 118 (12), 6448–6453.

(32) Joshi, H.; Ochoa-Hernández, C.; Nu¨renberg, E.; Kang, L.; Wang, F. R.; Weidenthaler, C.; Schmidt, W.; Schu¨th, F. Insights into the Mechanochemical Synthesis of Sn-β: Solid-State Metal Incorporation in Beta Zeolite. Microporous Mesoporous Mater. 2020, 309, 110566.

(33) Dijkmans, J.; Gabriëls, D.; Dusselier, M.; De Clippel, F.; Vanelderen, P.; Houthoofd, K.; Malfliet, A.; Pontikes, Y.; Sels, B. F. Productive Sugar Isomerization with Highly Active Sn in Dealuminated β Zeolites. Green Chem. 2013, 15 (10), 2777–2785.

(34) Astorino, E.; Peri, J. B.; Willey, R. J.; Busca, G. Spectroscopic Characterization of Silicalite-1 and Titanium Silicalite-1. J. Catal. 1995, 157 (2), 482–500.

(35) Dijkmans, J.; Dusselier, M.; Janssens, W.; Trekels, M.; Vantomme, A.; Breynaert, E.; Kirschhock, C.; Sels, B. F. An Inner-/Outer-Sphere Stabilized Sn Active Site in β-Zeolite: Spectroscopic Evidence and Kinetic Consequences. ACS Catal. 2016, 6 (1), 31–46.

(36) Sarr, B.; Diop, C. A. K.; Sidibé, M.; Rousselin, Y. Crystal Structure of Bis(Diisopropylammonium) Cis -Diiodidobis(Oxolato- K2 O1, O2)Stannate(IV). Acta Crystallographica Section E: Crystallographic Communications 2018, 74 (4), 502–504.

(37) Teutsch, U.; Schmidtke, H. H. On the Problem of Assigning Electronic Transitions in Diketonate Complexes. Polarized Crystal Spectra of Tin(IV) and Antimony(V) Mono(Acetylacetonate) and -(Tropolonate) Complexes. J. Chem. Phys. 1986, 84 (11), 6034–6047.

(38) Tian, Q.; Zhuang, J.; Wang, J.; Xie, L.; Liu, P. Novel Photocatalyst, Bi 2Sn 2O 7, for Photooxidation of As(III) under Visible-Light Irradiation. Applied Catalysis A: General 2012, 425–426, 74–78.

(39) Chiker, F.; Nogier, J. P.; Launay, F.; Bonardet, J. L. New Ti-SBA Mesoporous Solids Functionnalized under Gas Phase Conditions: Characterisation and Application to Selective Oxidation of Alkenes. Applied Catalysis A: General 2003, 243 (2), 309–321.

(40) Majoul, N.; Aouida, S.; Bessaïs, B. Progress of Porous Silicon APTES-Functionalization by FTIR Investigations. Appl. Surf. Sci. 2015, 331, 388–391.

(41) White, L. D.; Tripp, C. P. Reaction of (3-Aminopropyl)-Dimethylethoxysilane with Amine Catalysts on Silica Surfaces. J. Colloid Interface Sci. 2000, 232 (2), 400–407.

(42) Courtney, T. D.; Chang, C. C.; Gorte, R. J.; Lobo, R. F.; Fan, W.; Nikolakis, V. Effect of Water Treatment on Sn-BEA Zeolite: Origin of 960 Cm-1 FTIR Peak. Microporous Mesoporous Mater. 2015, 210, 69–76.

(43) Bell, J. V.; Heisler, J.; Tannenbaum, H.; Goldenson, J. Infrared Spectra of Metal Isopropoxides. Anal. Chem. 1953, 25 (11), 1720–1724.

(44) Bradley, D. C.; Lewis, J.; Thomas, I. M. et al. 2601 510. 1961, 2601–2605.

(45) Lynch, C. T.; Mazdiyasni, K. S.; Smith, J. S.; Crawford, W. J. Infrared Spectra of Transition Metal Alkoxides. Anal. Chem. 1964, 36 (12), 2332–2337.

(46) Kaya, M.; Baran, T.; Mentes, A.; Asaroglu, M.; Sezen, G.; Tozak, O. K. Extraction and Characterization of α -Chitin and Chitosan from Six Different Aquatic Invertebrates. Food Biophysics 2014, 9, 145–157.

(47) Khan, A. S.; Khalid, H.; Sarfraz, Z.; Khan, M.; Iqbal, J.; Muhammad, N.; Fareed, M. A.; Rehman, I. U. Vibrational Spectroscopy of Selective Dental Restorative Materials. Appl. Spectrosc. Rev. 2017, 52 (6), 507–540.

(48) Marchessault, R. H.; Pearson, F. G.; Liang, C. Y. Infrared Spectra of Crystalline Polysaccharides. Biochim. Biophys. Acta 1960, 45, 499–507.

(49) Morimoto, T.; Imai, J.; Nagao, M. Infrared Spectra of N-Butylamine Adsorbed Silica-Alumina. journal of Physical Chemistry 1974, 78, 704–708.

(50) Turishchev, S. Y.; Chuvenkova, O. A.; Parinova, E. V.; Koyuda, D. A.; Chumakov, R. G.; Presselt, M.; Schleusener, A.; Sivakov, V. XPS Investigations of MOCVD Tin Oxide Thin Layers on Si Nanowires Array. Results in Physics 2018, 11, 507–509.

(51) Jeong, M.; Yokoshima, T.; Nara, H.; Momma, T.; Osaka, T. Influence of the Diffusion-Layer Thickness during Electrodeposition on the Synthesis of Nano Core/Shell Sn-O-C Composite as an Anode of Lithium Secondary Batteries. RSC Adv. 2014, 4 (51), 26872–26880.

(52) Shircliff, R. A.; Stradins, P.; Moutinho, H.; Fennell, J.; Ghirardi, M. L.; Cowley, S. W.; Branz, H. M.; Martin, I. T. Angle-Resolved XPS Analysis and Characterization of Monolayer and Multilayer Silane Films for DNA Coupling to Silica. Langmuir 2013, 29, 4057.

(53) Dong, W.; Li, H.; Xi, J.; Mu, J.; Huang, Y.; Ji, Z.; Wu, X. Reduced TiO2 Nanoflower Structured Photoanodes for Superior Photoelectrochemical Water Splitting. J. Alloys Compd. 2017, 724, 280–286.

(54) Ma, J. W.; Lee, W. J.; Bae, J. M.; Jeong, K. S.; Oh, S. H.; Kim, J. H.; Kim, S. H.; Seo, J. H.; Ahn, J. P.; Kim, H.; Cho, M. H. Carrier Mobility Enhancement of Tensile Strained Si and SiGe Nanowires via Surface Defect Engineering. Nano Lett. 2015, 15 (11), 7204–7210.

(55) Mania, P.; Verel, R.; Jenny, F.; Hammond, C.; Hermans, I. Thermal Restructuring of Silica-Grafted TiClx Species and Consequences for Epoxidation Catalysis. Chem. - Eur. J. 2013, 19 (30), 9849–9858.

(56) Min, H.; Girard-Lauriault, P. L.; Gross, T.; Lippitz, A.; Dietrich, P.; Unger, W. E. S. Ambient-Ageing Processes in Amine Self-Assembled Monolayers on Microarray Slides as Studied by ToF-SIMS with Principal Component Analysis, XPS, and NEXAFS Spectroscopy. Anal. Bioanal. Chem. 2012, 403 (2), 613–623.

(57) Kulszewicz-Bajer, I.; Proń , A.; Abramowicz, J.; Jeandey, C.; Oddou, J. L.; Sobczak, J. W. Lewis Acid Doped Polyaniline: Preparation and Spectroscopic Characterization. Chem. Mater. 1999, 11 (3), 552−556.

(58) Maachou, H.; Genet, M. J.; Aliouche, D.; Dupont-Gillain, C. C.; Rouxhet, P. G. XPS Analysis of Chitosan-Hydroxyapatite Biomaterials: From Elements to Compounds. Surf. Interface Anal. 2013, 45 (7), 1088−1097.

(59) Farfan-Arribas, E.; Madix, R. J. Characterization of the Acid-Base Properties of the TiO2(110) Surface by Adsorption of Amines. J. Phys. Chem. B 2003, 107 (14), 3225−3233.

(60) Head, A. R.; Chaudhary, S.; Olivieri, G.; Bournel, F.; Andersen, J. N.; Rochet, F.; Gallet, J. J.; Schnadt, J. Near Ambient Pressure X-Ray Photoelectron Spectroscopy Study of the Atomic Layer Deposition of TiO2 on RuO2(110). J. Phys. Chem. C 2016, 120 (1), 243−251.

(61) Sardo, M.; Afonso, R.; Juźków, J.; Pacheco, M.; Bordonhos, M.; Pinto, M. L.; Gomes, J. R. B.; Mafra, L. Unravelling Moisture-Induced CO2 Chemisorption Mechanisms in Amine-Modified Sorbents at the Molecular Scale. Journal of Materials Chemistry A 2021, 9 (9), 5542−5555.

(62) Tielens, F.; Gierada, M.; Handzlik, J.; Calatayud, M. Characterization of Amorphous Silica Based Catalysts Using DFT Computational Methods. Catalysis Today 2020, 354, 3–18. https://doi.org/https://doi.org/10.1016/j.cattod.2019.03.062.

Chapter 3

Theoretical Mechanism and Activity of Open Defect and Closed sites in Sn-BEA for Epichlorohydrin Ring Opening Reaction with Alcohol

Sam Holton, Ambarish Kulkarni

Introduction

Regioselective catalysis has significant applications in the solvent and pharmaceutical industries, and has been demonstrated in a wide variety of homogeneous systems. Regioselective reactions are essential for producing high quality solvents, plastics, drugs and other fine chemicals. However, developing regioselective heterogeneous catalysts has been a long standing challenge. Currently, regioselective products are produced by leveraging the inherent regioselectivity of certain reactions, by using homogeneous catalysts, or via column separations. Alcohol ring opening of epichlorohydrin is one such reaction where it would be highly valuable to catalyze as epichlorohydrin is used for polymer synthesis and epoxy resin production.

Zeolites are a common, versatile catalyst support that may be promising for regioselective catalysis. Regioselective reactions over zeolites have been demonstrated. Closed sites are the most commonly studied configuration of the framework tin atom while hydrolyzed open and open defect sites are implicated in some reactions.

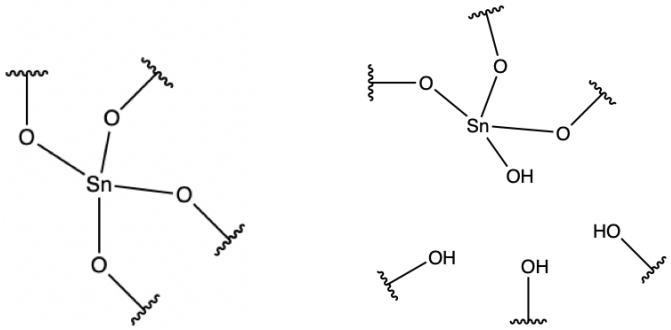

Scheme 1. Closed (left) and open defect sites (right).

Motivated by experimental results showing higher activity for an open defect material, we use DFT to study the epichlorohydrin ring-opening reaction over closed and open defect sites in Sn-BEA. We compute energy curves and reaction barriers for the reaction over closed and open defect sites in BEA and find that closed sites have favorable activity compared to open defect sites due to their weaker methanol binding facilitating proton transfers.

Results

Previous results in the group have found significant differences between Sn-BEA catalysts synthesized with a tin precursor versus a methyl tin precursor despite the fact that both catalysts were calcined12 (thus removing the methyl group). This suggests that the methyl group changes the tin active site; it has been theorized that calcination of Me-Sn-BEA generates tin sites with an adjacent silanol nest group (open site).

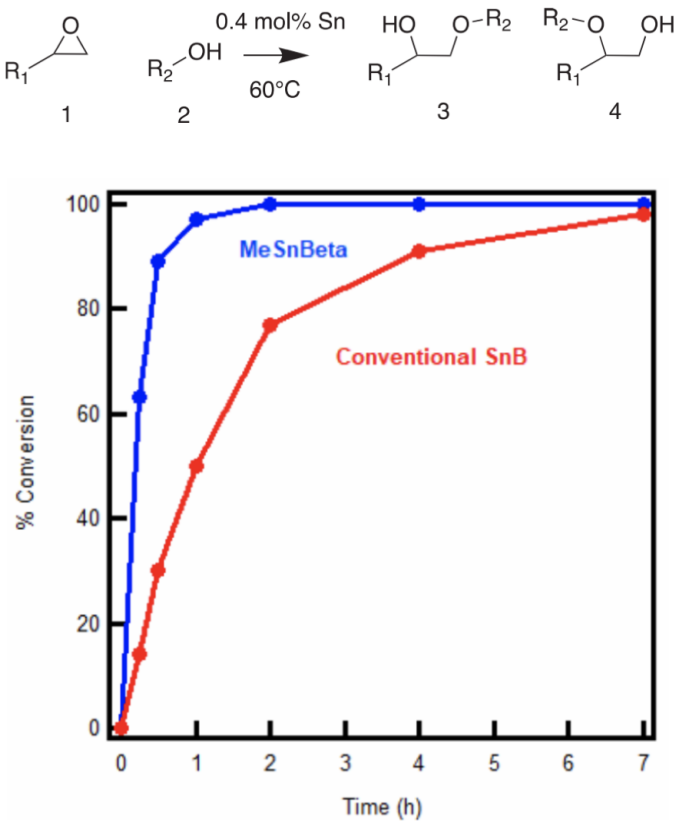

Figure 1. Experimental Conversion vs. Time for the alcohol ring opening reaction of epichlorohydrin. Sn-BEA synthesized with a methyl precursor shown in blue, and with a conventional $SnCl_4$ precursor shown in red. Data collected by Dr. Alex Spanos and Prof. Nick Brunelli of Ohio State University.

To study this reaction, we first optimized the full silica unit cell of BEA using the crystal structure obtained from IZA. The optimized unit cell parameters were held constant for the remainder of the study. Next, we replaced an Si atom with a Sn atom at each of the 9 T-sites in BEA and optimized each structure to produce a closed Sn site. For each closed site, 4 possible open defect sites were prepared by removing an adjacent Si atom, capping the dangling oxygen atoms with a hydrogen atom to form silanols, and relaxing the structure. All structures were optimized using the VASP DFT package with the RPBE functional at a 500 eV ENCUT. Figure 2

shows the relative energies of the four possible placements of the silanol nest for each T-site. Because of the differences in energy, we used only the open site configurations with the lowest energy for subsequent for the remainder of the study.

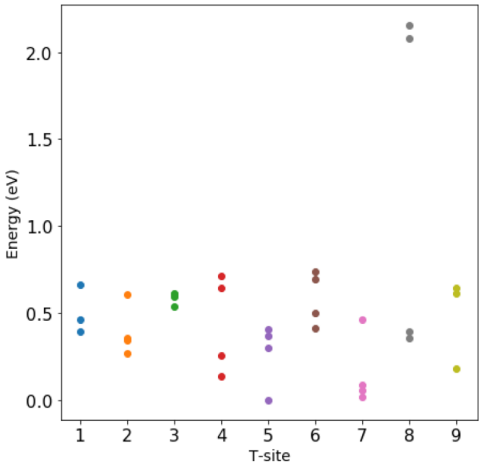

Figure 2. Relative energy of the four silanol nest positions for open defect sites in Sn-BEA.

Next, we considered the possible mechanisms of the epichlorohydrin ring opening reaction in the presence of methanol. The first mechanism we considered involved a single methanol bound to the tin atom acting as both the proton donor and the nucleophile. Next, we considered the same mechanism using a methanol dissociated over the tin site, with its proton on a framework oxygen atom. Alternatively, a second, unbound methanol molecule could act as the nucleophile while the bound methanol donates a proton. Like the 1-methanol case, we considered mechanisms where the bound methanol was either intact or dissociated.

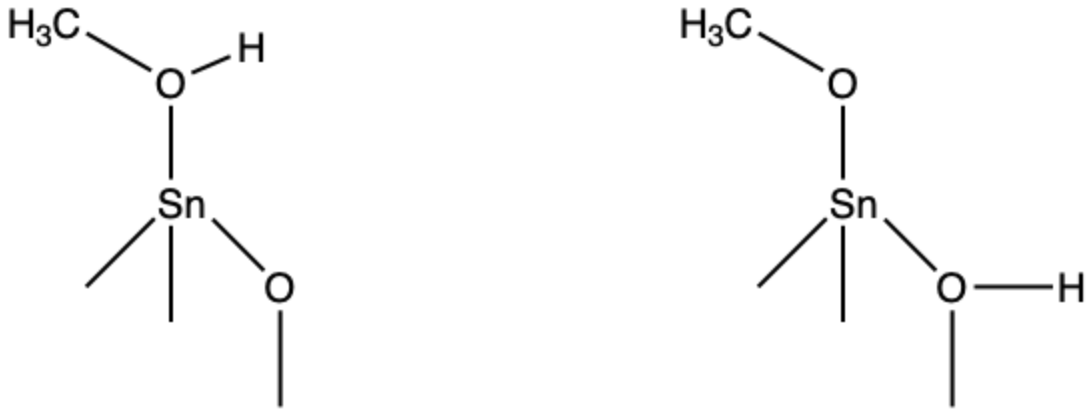

Scheme 2. (Left) **"**Intact" methanol with a proton on the methoxy group. (Right) "Dissociated" methanol with the proton on a framework oxygen atom.

To determine which mechanism was the most likely, we used the T9 site as a representative system and performed Nudged Elastic Band calculations for each mechanism. Fig 3 shows the barriers for various mechanisms. The 2-methanol mechanism had the lowest barrier of 0.73 eV for the open defect site and 0.93 eV for the closed site.

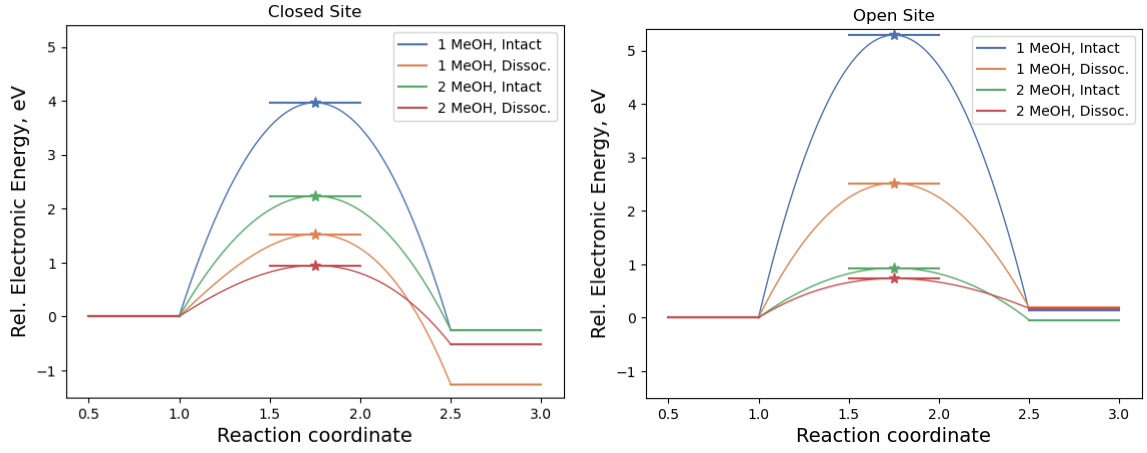

Figure 3. Relative electronic energy barriers for the 4 studied mechanisms over the Closed and Open Defect sites.

The 2-methanol dissociated mechanism had much lower barriers than the other mechanisms, suggesting it is the most plausible way for the reaction to proceed. We can put the reaction into context by considering the full energy curve for open defect and closed sites on the T9 site in Figure 4 below. The open site more readily dissociates methanol and has a lower electronic energy barrier.

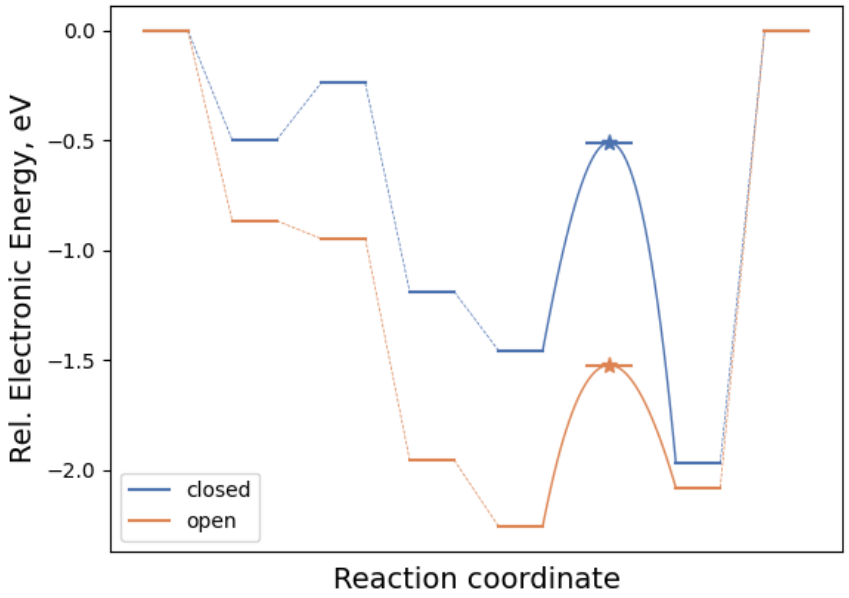

Figure 4. Full energy curves for Epichlorohydrin ARO over closed and open sites. The reaction intermediates are: bare site, methanol binding, methanol dissociation, 2nd methanol addition, epichlorohydrin addition, and final product. The star denotes the transition state.

To see how these results generalize to other T-sites, we repeated the nudged elastic band calculations on all closed and open sites for this mechanism. We had difficulties binding intermediates to the T5 and T6 sites due to their position in the framework, so they were excluded from the remainder of the study. The results are shown in figure 5 and the Supplementary Table. Unlike the T9 site, most other T-sites have lower electronic energy barriers

for the closed site. In fact, the closed T8 site exhibits the lowest barrier to reaction with 0.63 eV. As many of the barriers are significantly higher than the T8 site, the observed reaction rate is likely to be determined by the sites with the highest turnover frequency, such as closed-T8 and open-T9.

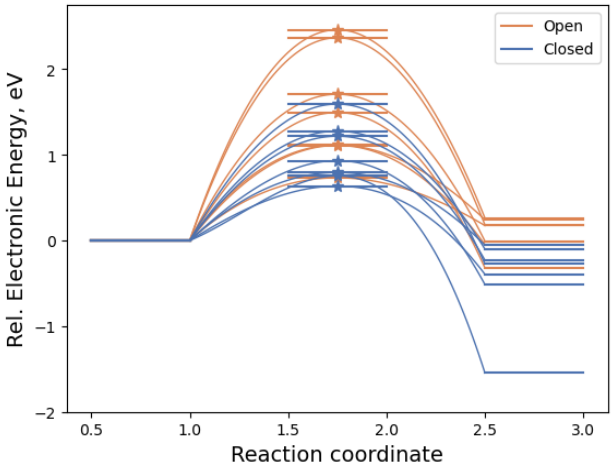

Figure 5. Relative electronic energy barriers for all closed and open defect sites.

With barriers for each T-site, we can consider whether the barrier height scales with the binding energy of methanol (Figure 6). Though it is difficult to draw strong conclusions from a handful of datapoints, the closed sites appear to bind methanol slightly weaker and exhibit lower reaction barriers.

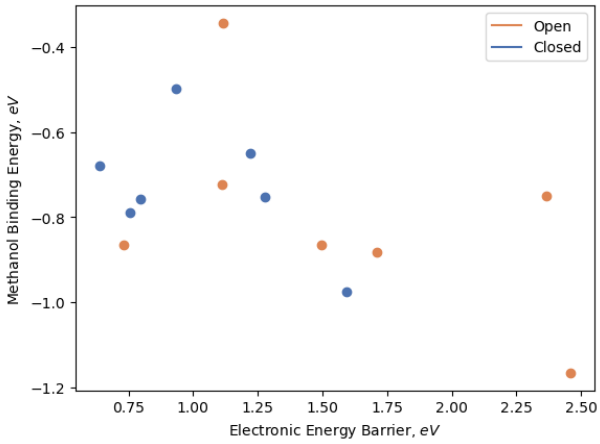

Figure 6. Relative electronic energy barriers Vs. methanol binding energy for all closed and open defect sites.

Discussion

Closed sites show increased activity for epichlorohydrin alcohol ring opening. Across T-sites, the activation barrier is lower over closed sites than the corresponding open site. Weaker methanol binding at closed sites may facilitate proton transfer, explaining the observed trend.

Considering these findings, the improved turnover frequency in the Me-Sn material remains a mystery. Presumably, open defect sites are present in the material, but theory suggests that closed sites exhibit higher activity. The open defect sites may undergo a transformation during calcination, creating a structure that wasn't considered in this work. The condensed open site considered in Chapter 1 is one such possibility; the bridging silanol has been observed to transfer a proton to the Sn-OH group in some situations, creating a water molecule which may be removed during calcination. This would produce a framework bound tin similar to a closed site with one longer Sn-O bond and possessing different reactivity.

The gas-phase treatment presented here also neglects solvation effects. The presence of the silanol nest may coordinate with solvent molecules, changing the environment around the active site and facilitating proton transfers, potentially lowering the reaction barrier.

Conclusions

We examined the thermodynamic feasibility of creating open defect Sn sites in BEA and their catalytic properties with respect to the epichlorohydrin ring opening reaction. We find that open sites possess worse reaction kinetics for this; the presence of an adjacent silanol nest may stabilize the dissociated methanol, hindering the proton transfer step.

This line of research could be extended to other zeolite topologies, metals, and reactions. While this work was carried out under the assumption of a gas phase reaction, studying this reaction in solution-phase would be valuable. The effects of the silanol nest on solvent coordination, reaction environment, and reaction mechanism may be considerable. Our results leave open the possibility of another type of active site present in the Me-Sn material with improved activity.

Supplementary Table

T-site	Closed Barrier (eV)	Open Barrier (eV)
1	0.76	1.71
2	1.59	1.5
3	1.28	2.46
4	1.22	1.11
7	0.80	1.12
8	0.63	2.37
9	0.93	0.73

Chapter 4

Characterizing Tin Site Speciation in Zeolite Beta Using TMPO NMR Probes

Sam Holton, Ambarish Kulkarni

Introduction

Sn-Beta is a zeolite catalyst commonly used in industry of interest for applications in biomass conversion. Different synthesis conditions can prepare the atomically dispersed tin site in a closed, hydrolyzed open, and defect open configuration, each with distinct catalytic activities.

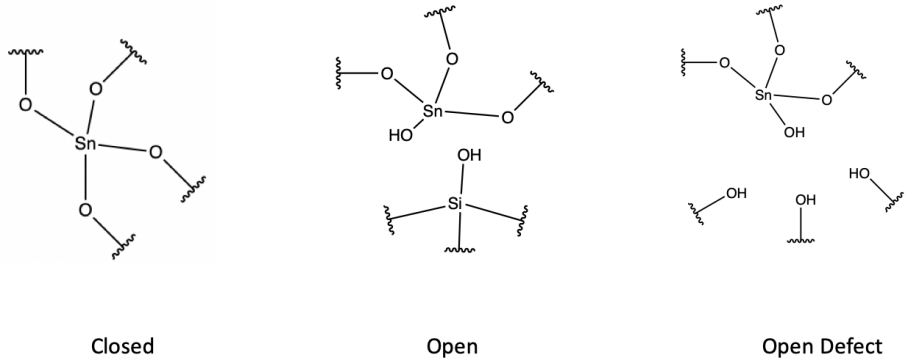

Scheme 1. Closed, Open, and Open Defect sites. Cutoffs indicate binding to the zeolite framework.

However, the development of synthetic techniques to produce specific Sn sites is hampered by the difficulty of characterizing Sn speciation in zeolites. Without the ability to determine which sites are present in a material, it is difficult to validate different synthetic techniques.

Previously, researchers have used solid-state magic angle spinning NMR on ^{119}Sn nuclei to identify different states of the tin atom in zeolites. Bates et. al. used tin NMR to identify closed and open defect sites, and identify distinct catalytic activity for each site. These experiments

provide us detailed information about tin sites, but are difficult to carry out and are hard to generalize to other acid sites without spin-active nuclei.

Infrared spectroscopy has also been used to characterize acid sites in zeolites. CO, NO, and acetonitrile bind to acid sites in zeolites and change their characteristic frequency in response to the type and strength of the acid site. These experiments have the benefit of being easier to run, at the cost of being harder to interpret due to broad peaks containing many different acid sites.

One way to balance the simplicity of molecular probe techniques with the sophistication of NMR is to use NMR active probe molecules. For example, phosphorus-containing molecules such as tri-methyl phosphine and trimethyl-phosphine oxide have been used as acidity scales for Brønsted acid sites and have been used to compare the Lewis-acidity of different zeolites. The high elemental abundance and sensitivity of the ^{31}P nucleus makes NMR experiments more accessible and the insertion of a probe guarantees the presence of a spin-active nucleus in the material, making NMR experiments possible for any zeolite.

Inspired by the use of TMPO as an NMR probe for Bronsted- and Lewis-acidity, we consider whether TMPO can be used to distinguish open and closed sites in BEA. We start with experimental data showing two distinct peaks in the TMPO NMR spectra. We then theoretically validate TMPO as an NMR probe by computing NMR for all possible open and closed sites in BEA, conducting a detailed study of the T9 site. The referenced NMR matches experiment, confirming that TMPO is a useful NMR probe for distinguishing Sn site speciation in zeolite catalysts.

Experimental Results

Our experimental collaborators Dr. Alex Spanos and Professor Nick Brunelli from OSU conducted ^{31}P TMPO NMR experiments on two zeolite Sn-Beta (BEA) materials. One was synthesized with a traditional tin precursor while the other was synthesized using a methyl tin precursor intended to create a silanol nest site adjacent to the tin after calcination. Figure 1 shows the TMPO NMR spectra for the traditional synthesis in blue, with the methyl-tin synthesis in red.

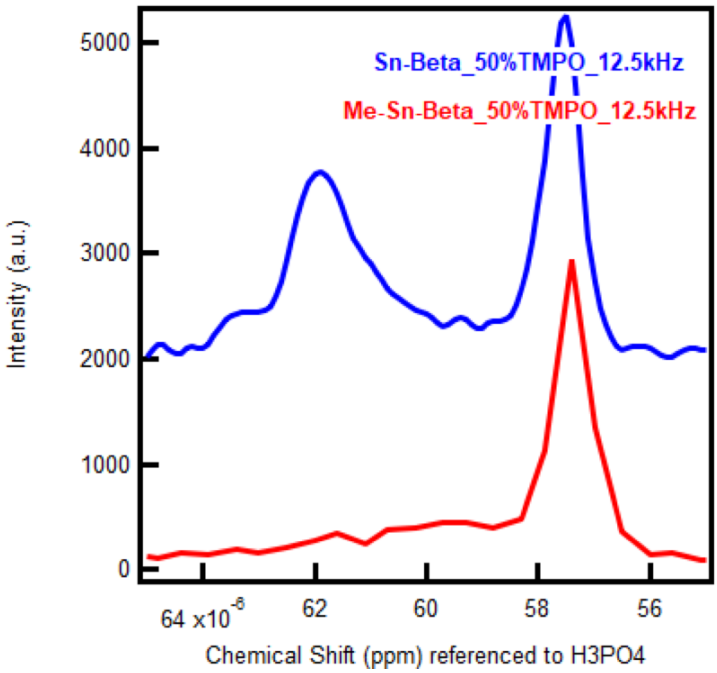

Figure 1. ^{31}P NMR of TMPO molecule adsorbed to traditionally synthesized Sn-BEA (blue) and Sn-BEA synthesized with a methyl-Sn precursor (red).

In both cases, the amount of TMPO added was half the amount of tin used in the synthesis. The spectra had no other peaks in the relevant region, suggesting that these peaks come from TMPO molecules bound to the tin atom.

The spectra suggests that the traditional synthesis resulted in two different tin speciations, while the methyl tin precursor selectively produced a single tin speciation. Our goal is to investigate the tin active sites in these catalysts.

Methods

To study TMPO as an NMR probe in BEA, we first obtained the BEA unit cell from the IZA database and performed a full unit cell optimization with the lattice parameters held fixed for the remainder of the study. Next, we prepared closed Sn site configurations within BEA by placing a tin atom at each of nine the crystallographically distinct T-sites and optimizing these structures. For each closed site, we optimized 4 possible open defect sites; using the MAZE code to replace one of the four adjacent framework silicon atoms with a silanol nest. For the remainder of the study, we focused on the open site configuration with the lowest energy, retaining one open site for each T-site.

Next, we added a TMPO molecule bound to the tin in each open and closed structure and optimized the structure. All periodic optimizations were performed in VASP with the RPBE functional with 500 eV ENCUT (See figure 5).

To select a functional to optimize the cluster geometries and compute NMR, we conducted a bond scan calculation on the T9 site. Starting with clusters derived from the periodic closed, open defect, and condensed open site, the Sn-TMPO distance was held fixed at various distances while the rest of the structure was allowed to relax. Figure 2 compares the relative energy curves for each structure computed with PBE, PBE0, and M06L functionals. These are compared to

"gold-standard" DLPNO-CCSD(T) single point energies computed on the PBE0 and M06L structures. Convergence issues prevented us from computing bond scans using CCSD(T) optimized structures.

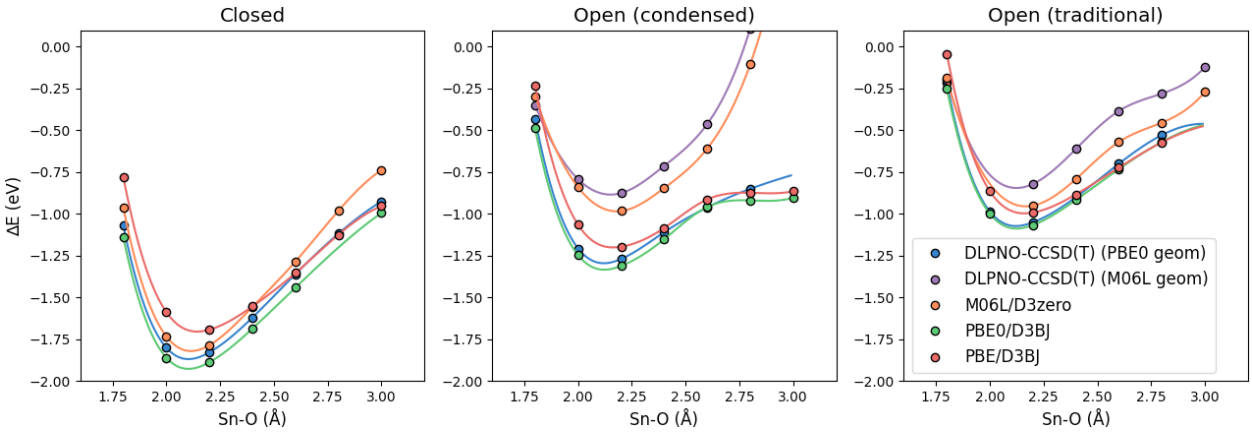

Figure 2. Bond scans of relative electronic energy with increasing Sn-TMPO distance for various functionals.

PBE0 is in good agreement with the corresponding bond scan computed with CCSD(T), with PBE showing similar trends. M06L obeys similar trends to the corresponding bond scan computed with CCSD(T) with erratic behavior at longer bond lengths.

To further compare these functionals, we computed NMR parameters for the open and closed sites at each point in the bond scans. PBE and PBE0 follow a similar pattern, while M06L reverses the ordering of open and closed nuclear isotropic shielding and displays erratic behavior (fig 3).

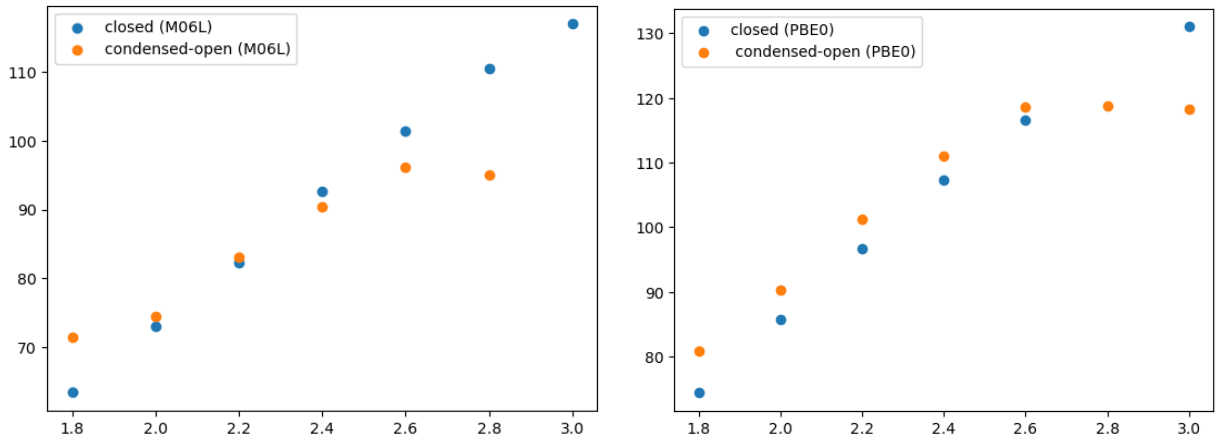

Figure 3. ^{31}P TMPO NMR vs. Sn-TMPO distance, illustrating the erratic behavior of M06L.

Experimentally, it appears that open sites have a lower referenced shift, making PBE and PBE0 more consistent with the experimental trend. Given the erratic behavior at bond lengths away from equilibrium and the inconsistency with the experimental trend, we decided to exclude M06L from further analysis.

We then benchmarked PBE, PBE0, and DSD-PBEp86 functionals against a dataset of organotin-TMPO complexes observed with solution-phase NMR.

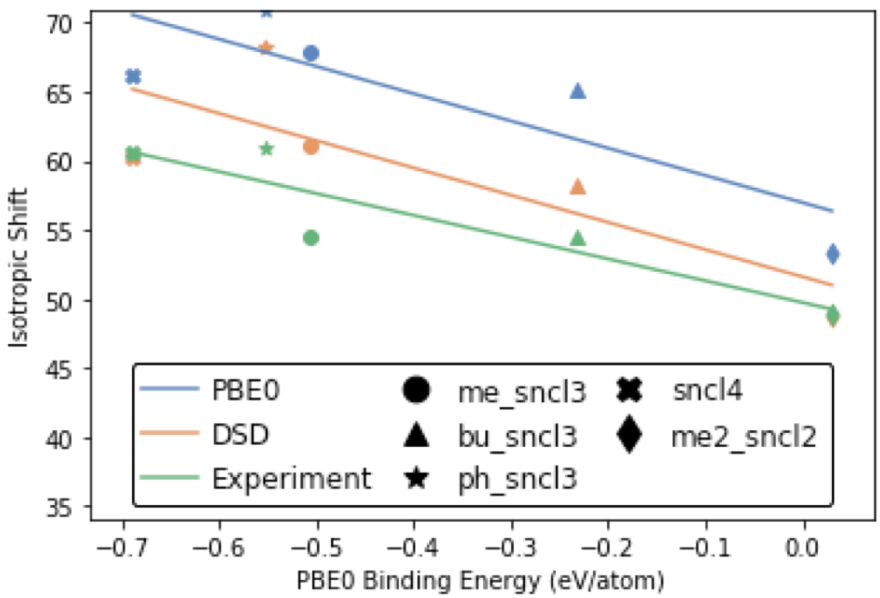

Figure 4. PBE0 Binding energy vs. isotropic shift for experimental and calculated values.

Though DSD-PBEp86 outperformed PBE0 in an absolute sense, PBE0 NMR appears to match the experimental trend properly and is correct up to a constant shift. Due to some convergence issues with DSD-PBEp86, and the accuracy of PBE0 geometries, we decided to use the PBE0 functional for the remainder of the study.

To compute ^{31}P NMR spectra for each configuration, we selected the ORCA package. This package computes properties for non-periodic systems, so we needed to obtain a representative local environment for each active site. To do so, we used the MAZE package to remove a 5T cluster centered around the Tin atom and capped the unsaturated oxygen atoms with hydrogen atoms, forming silanol groups.

Next, we relaxed the hydrogen atoms using the ORCA package while keeping the other atoms fixed. Next, the peripheral hydrogen atoms, silicon atoms, and peripheral oxygen atoms were held fixed while the rest of the cluster was allowed to relax. This was done in order to retain the shape of the original periodic structure while allowing the local environment of the Sn to relax. NMR was computed for each T-site and referenced to the gas phase value.

Results

The binding energies of TMPO in the full BEA unit cell were computed with VASP and are shown in figure 5a. The binding energies and Isotropic shifts were also calculated in ORCA and are shown in figure 5b.

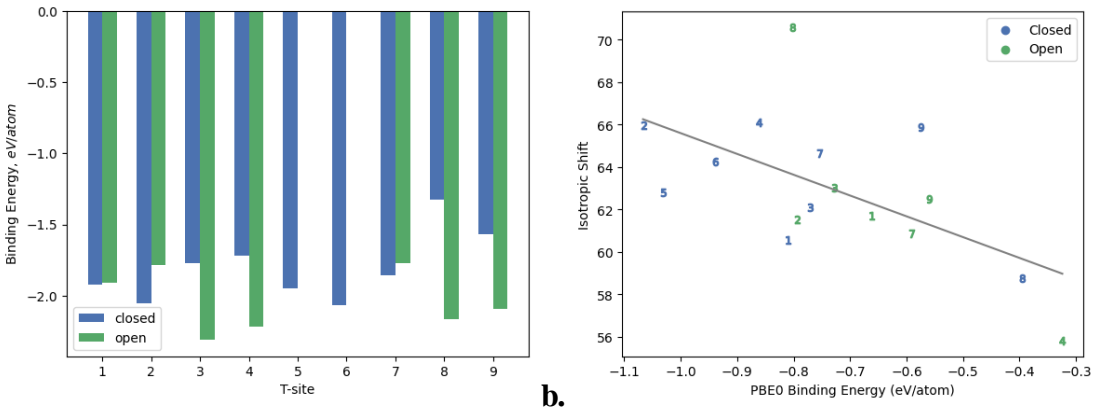

a. **b.**

Figure 5. (a)TMPO binding energy for open and closed sites computed with VASP. **(b)** TMPO binding energy vs. isotropic shift computed with ORCA.

With the exception of the T8 site, the closed sites generally had higher isotropic shifts and more negative binding energies. Note the correlation between binding energies and isotropic shift. Closed site isotropic shifts centered around 65 ppm and while open sites centered around 62

ppm. This follows the same trend as experiment, but DFT appears to overestimate the isotropic shifts by roughly 4 ppm. Note that optimized structures correspond to zero Kelvin equilibrium geometries which are not representative of a room temperature experiment. This issue will be addressed in the next section.

In the process of preparing these structures, we observed two different types of open sites. After optimization, most sites possessed a disconnected silanol nest as expected for an open defect site. However, some sites such as the T9 site formed an additional bond between a silanol and the tin atom, producing an octahedral coordination. This rearrangement occurred spontaneously, increasing the stability and will be referred to as a "condensed open site". We conducted a detailed investigation of the T9 site in 3 possible configurations: closed, (traditional) open, and condensed open.

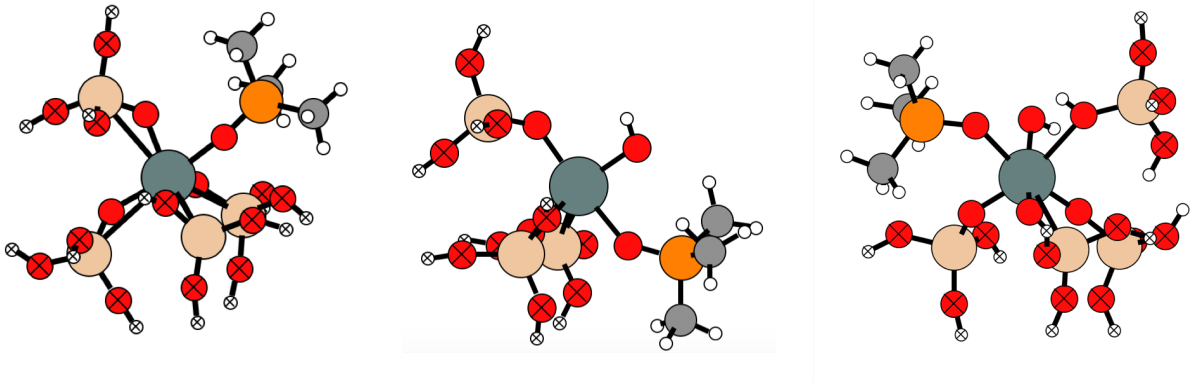

Figure 6. Closed (left), traditional open defect (center), and condensed open defect (right) sites bound to TMPO. Shown as 5T cluster models for simplicity.

To ensure that our conclusions are robust to DFT errors in the geometry, we reoptimized the geometry and computed NMR at various Sn-O distances. Figure 7 shows that as the Sn-TMPO distance is extended, all sites show steady changes in other geometric parameters such as the P-O distance.

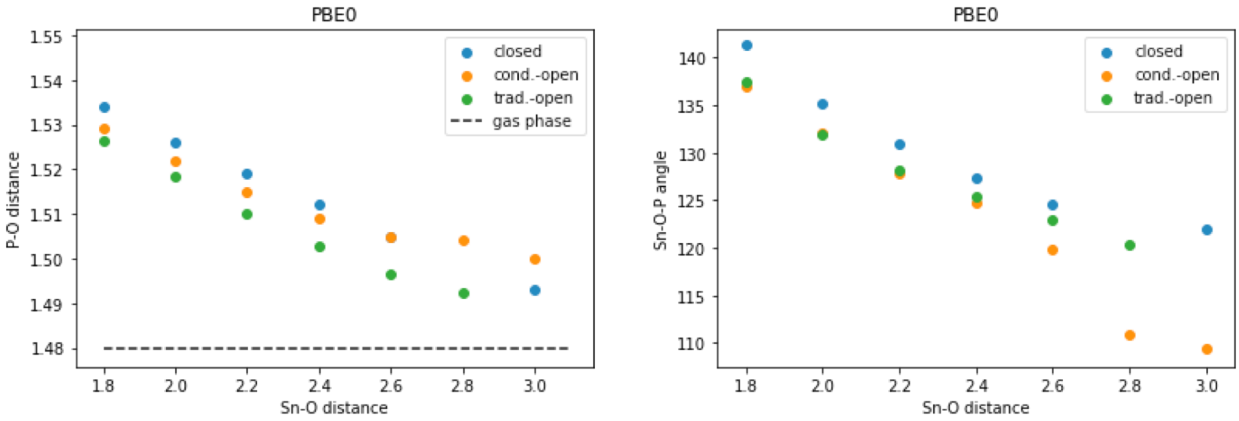

Figure 7. Geometric changes to the Sn-TMPO system during a bond scan.

These differences in geometry translated into consistent changes in NMR parameters across a range of bond lengths (fig 8). The ordering relative to gas phase TMPO remained the same. Near the equilibrium distance, the closed and condensed open site differed by 4 ppm while the traditional open site was 8 ppm higher than the closed site.

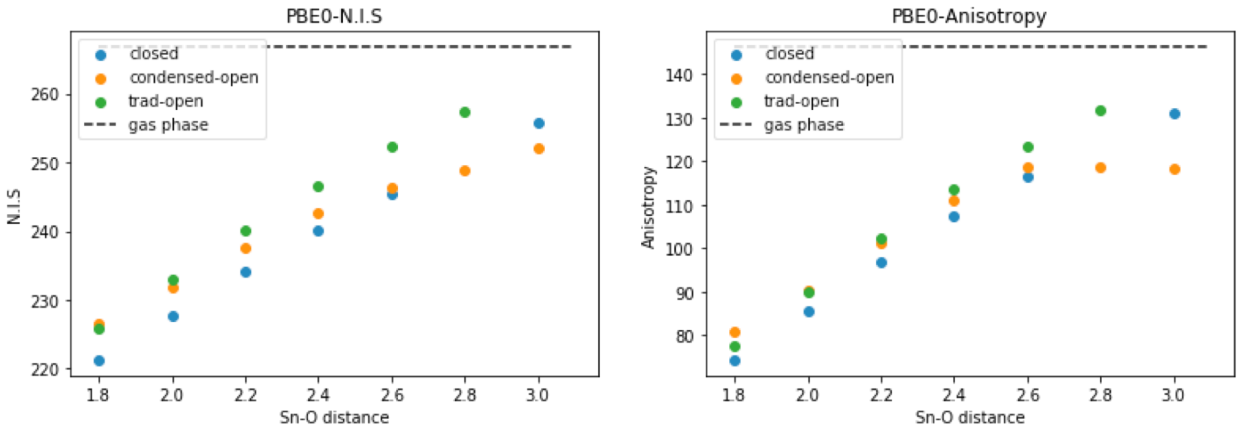

Figure 8. Changes in TMPO NMR during a bond scan.

While the bond scan illustrates changes in NMR parameters across a range of geometries, the experimental NMR signal comes from the Sn-TMPO system moving dynamically about its equilibrium bond length. We ran a molecular dynamics simulation of TMPO in the full Sn-BEA unit cell to simulate realistic geometries of the Sn-TMPO system. We then sampled the series of configurations at regular intervals, produced 5T cluster models of selected configurations, and computed NMR for each geometry. Figure 9 displays a histogram of the sampled N.I.S. for open, condensed open, closed, and unbound TMPO. Similar to the bond scans, open and closed sites exhibited a 6 ppm difference, with open sites closer to the reference. Interestingly, the gap between open and condensed open sites disappeared.

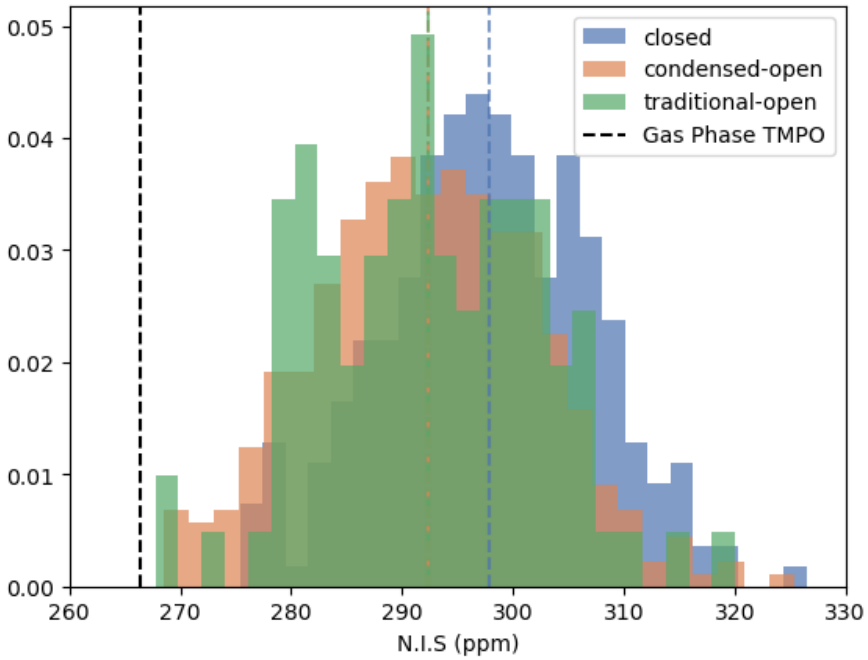

Figure 9. Histogram of computed nuclear isotropic shieldings for sampled configurations from MD on the T9 site.

We then repeated this procedure for all T-sites, combining open site and condensed open site data under the same category. Figure 10 shows histograms of the N.I.S. data. The averages of the open and closed sites differ by 4 ppm, with open sites closer to gas phase TMPO.

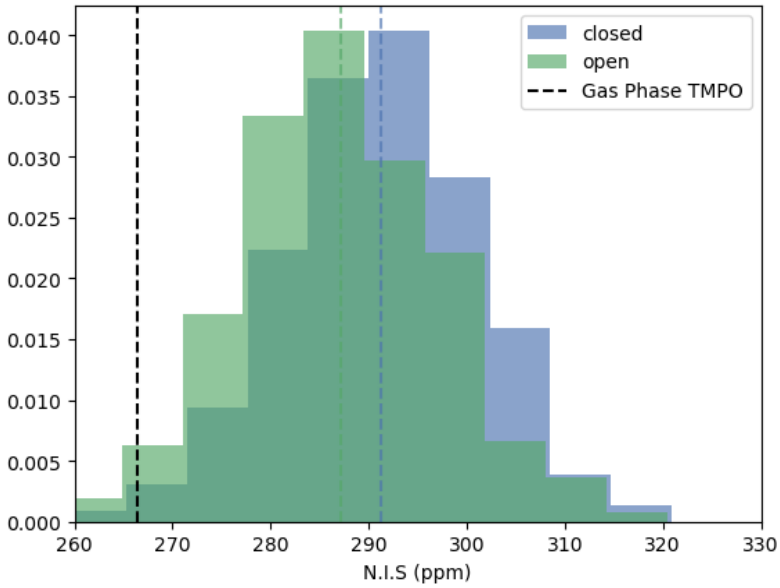

Figure 10. Histogram of computed nuclear isotropic shieldings for sampled configurations from MD for all T-sites.

Discussion

Across the bond scan, cluster models, and molecular dynamics studies, open sites exhibit NMR shifts that are 4-10 ppm closer to reference (lower) than closed sites. The most advanced modeling using molecular dynamics suggests that open sites should be 6 ppm lower than closed sites when referenced to gas-phase TMPO. This is consistent with experimental data showing two peaks 6 ppm apart in Sn-BEA synthesized with a traditional precursor. In Sn-BEA synthesized with a methyl-tin precursor, only the peak consistent with the open defect site is present, suggesting that open defect tin sites have been predominantly produced.

From these results, it appears that TMPO can distinguish open defect sites and closed sites in Sn-BEA.

Conclusion

Experimental TMPO NMR of two different tin precursors for Sn-BEA revealed two distinct tin speciations. We benchmarked different methods for computing ^{31}P NMR and then computed NMR for a variety of possible tin speciations. Across a variety of studies, open defect sites exhibited roughly 6 ppm lower NMR shift, consistent with experimental data suggesting that the methyl tin precursor preferentially created open defect sites. This suggests that TMPO may be a valuable NMR probe for characterizing tin speciation in zeolites.

Chapter 5

Theoretical Comparison Deuterated Acetonitrile IR and ^{15}N NMR for Characterizing Tin Sites in Zeolites

Authors: Samuel J. Holton, Dr. Alexander P. Spanos,a Dr. Nicholas A. Brunelli,*,a Dr. Ambarish Kulkarni*,b

Author address: a UC Davis; b William G. Lowrie Department of Chemical and Biomolecular Engineering, The Ohio State University, 151 West Woodruff Avenue, Columbus, OH 43210, U.S.A.

Introduction

Zeolites are an important class of industrially-relevant catalytic materials. They are stable, relatively cheap, and well-understood. Their properties can be modified via the addition of extra-framework cations, incorporation of transition metals into the framework, or by changing the composition of the framework. Since zeolites are nanoporous, additional control can be obtained by choosing a zeolite topology with an optimal window size (e.g., to control diffusion) and pore characteristics (e.g., large vs. small pore zeolites, channel vs. pockets) – this enables zeolites to be a versatile class of materials for several different applications.

Zeolites incorporating Sn, Ti, Hf, Zr, and Ge have been studied for a variety of Lewis acid catalyzed reactions [1]. Some processes of interest include biomass conversion, the MPV reaction, and fine chemicals synthesis. For instance, Deshpande et. al. reported high activity for

epoxide ring opening reaction with alcohols using a Sn-BEA catalyst [2]. While the active sites of zeolite catalysts have been studied, the origin of the nature of the catalytic site remains unknown in many cases.

Although several studies focused on optimizing catalytic performance are available in the literature, the identification and characterization of the active site responsible for the catalytic activity and selectivity remains challenging. A key complicating aspect is the fact that typical Sn-zeolite synthesis results in the formation of a mixture of Sn-sites. Additionally, as solvent effects are important for several Lewis acid catalyzed reactions, deconvoluting the effects of the pore hydrophobicity (which also depends on synthesis conditions) and Sn-speciation is not trivial.

While there exist techniques to measure the hydrophobicity of the material (e.g., using water adsorption), the identification of the catalytically active Sn-speciation is challenging due to the presence of multiple Sn sites – often in distinct crystallographic positions. As summarized in Fig. 2, closed, open and open-defect Sn-speciations are commonly studied in the literature. Each site has different catalytic activities and properties. Different synthetic methods purport to produce more of one speciation over the others; quantifying the Sn-speciation depends on the characterization method used to discriminate between the different sites.

Common methods for characterizing the Sn site rely on addition of a small molecule probe (e.g., deuterated acetonitrile (d-ACN), pyridine, trimethyl phosphine oxide (TMPO), trimethyl phosphine (TMP) or directly investigating the Sn local environment using ^{119}Sn NMR. While

FTIR spectroscopy (which probes the vibrational mode of the C-N bond) is most often used with d-ACN, phosphorus-based probes are usually coupled with ^{31}P NMR experiments. Although more advanced NMR techniques such DNP NMR have been developed, d-acn/FTIR remains a popular and simple approach to characterize Sn-sites.

For example, Vega-Vila et. al. theoretically and experimentally identified two peaks in the d-ACN spectra of Sn-CHA that were assigned to closed and open Sn sites [3]. Theoretical work by Bukowski et. al. confirmed that d-ACN bound to closed and open Sn sites exhibit different C-N stretch frequencies [4]. Using these known frequencies, the acetonitrile IR spectra can be deconvoluted to estimate the fraction of open and closed sites. Although d-ACN/FTIR remains popular, care must be taken to account for the presence of residual water, changes in the peak position with d-ACN loading, and the equilibration time prior to the FTIR data collection. Additionally, the peak deconvolution is often based on using fixed centers (i.e., 2308 and 2316 cm^{-1}) for the analysis.

When d-ACN binds to different Sn-sites within the zeolite, the interaction of the N electron lone pair with the Sn orbitals causes changes in the C-N stretching frequency (relative to gas phase d-ACN). Thus, for a given Sn-site, we hypothesize that stronger d-ACN binding will result in higher deviation (i.e., higher frequencies).

Notwithstanding the limitations of this simplistic model, the question arises if the difference between open and closed binding energies corresponds to only a small binding energy difference.

When we run adsorption energy calculations, we find that the open/closed binding is reversed. The overarching goal of this paper is to rationalize these differences.

Secondly, the above analysis is based on deconvolution differences in adsorption of only a few eV and a few tenths cm-1. The question is, if other characterization approaches can be used. Specifically, while ^{119}Sn and ^{31}P NMR have been used, ^{15}N NMR with d-ACN has only been used for cation exchanged zeolites. Nitrogen NMR is another common technique used to study Sn speciation. ^{15}N NMR has been used to study cations exchanged on zeolites as well as the Brønsted and Lewis acidity of different catalysts [5, 6]. Dib et. al. were even able to use nitrogen NMR to measure the degree of disorder in the nitrogen OSDA's as a proxy for the crystallinity of the synthesized zeolite [7]. Of particular interest is Harris et. al.'s use of Sn and ^{15}N pyridine NMR to determine the presence of closed and open defect Sn sites [8]. Thus, the second key goal of this paper is to demonstrate that ^{15}N NMR with acetonitrile is a very powerful technique.

Thus, the overall goal of this paper is to use density functional theory to assess the accuracy of acetonitrile IR and NMR in differentiating closed, open, and open defect Sn sites in CHA. We begin with a detailed study of different acetonitrile binding configurations in Sn-CHA. We find that once these configurations are accounted for, there is a significant spread in acetonitrile IR frequencies, making peak deconvolution difficult but still possible. We then study ^{15}N NMR on the same set of configurations. We find that NMR shieldings more clearly differentiate these three sites and the use of anisotropies computed from NMR spectra can be used to further identify these sites.

Results

Figure 1 shows a typical deuterated acetonitrile IR spectra in Sn-CHA. The large peak at 2310 cm^{-1} is usually deconvoluted into an open site peak at 2316 cm^{-1} and a closed site peak at 2308 cm^{-1}. By centering Gaussians at these positions and computing the relative contributions to the peak, an estimate of the relative amount of open and closed sites can be obtained. As the acetonitrile loading increases, the central peak shifts towards lower wavenumbers, indicating that the closed site more weakly binds the acetonitrile.

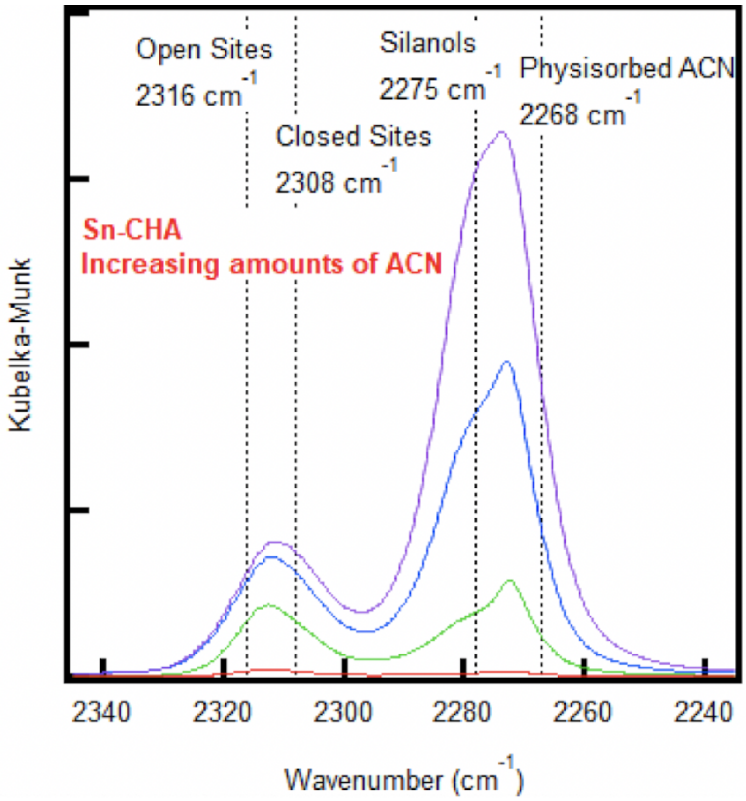

Figure 1. IR spectra of deuterated acetonitrile on Sn-CHA. Dotted lines indicate common peak locations.

To more fully understand this spectra, we began with a detailed study of the structures which compose these peaks. We begin by calculating the vibrational frequency of Sn-bound d-ACN in

Sn-substituted CHA. CHA was chosen as it has only 1 T-site, allowing us to isolate the effect of different Sn active sites and simplify our study considerably.

We considered 3 possible Sn speciations in Sn CHA: Closed sites, hydrolyzed open sites, and defect open sites (Fig. 2). Closed sites consist of a Sn atom participating in 4 bonds to framework oxygen atoms, replacing an Si atom. This is the most commonly studied zeolite active site. Hydrolyzed open sites differ from closed sites in that a single Sn-O bond has been hydrolyzed, resulting in an SnOH and a silanol group. Defect open sites involve a Sn atom adjacent to a missing-Si defect in the zeolite, leaving an SnOH group and 3 dangling SiOH groups in place of the missing Si atom. Though there is only 1 possible configuration for the closed site, there are 4 possible Sn-O bonds to replace with an OH group for each open site. Using DFT, we prepared all of these configurations in a full CHA unit cell and fully relaxed their structures in VASP using the PBE functional at 600 eV ENCUT.

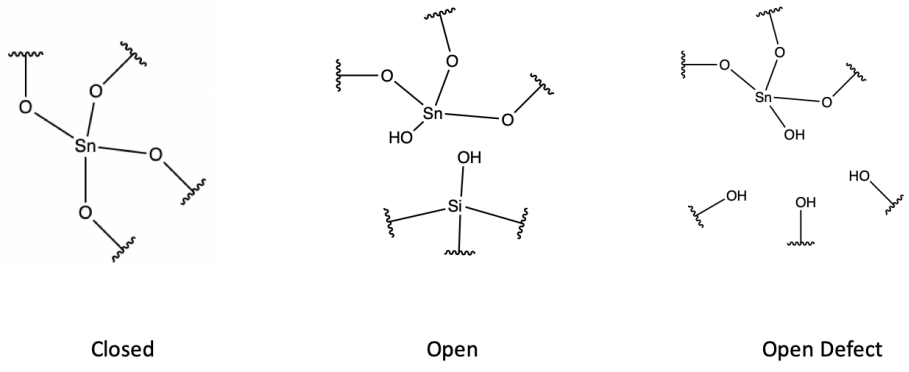

Figure 2. Closed, Open, and Open Defect sites. Cutoffs indicate binding to the zeolite framework.

Next, we placed an ACN molecule on a Sn atom of each type, optimized the geometry, and computed the vibrational frequencies for the CN stretch (see computational details). We also computed vibrational frequencies for gas phase ACN as well as 1 or 2 ACN's present in an all Si chabazite. The results are then referenced to experimental gas phase frequencies and compared to experiment in Figure 3. It is clear that though the closed and physisorbed ACN frequencies are in good agreement with experiment, the open site frequencies are far away from their expected value. More concerning, the trend between open and closed sites is reversed relative to experiment.

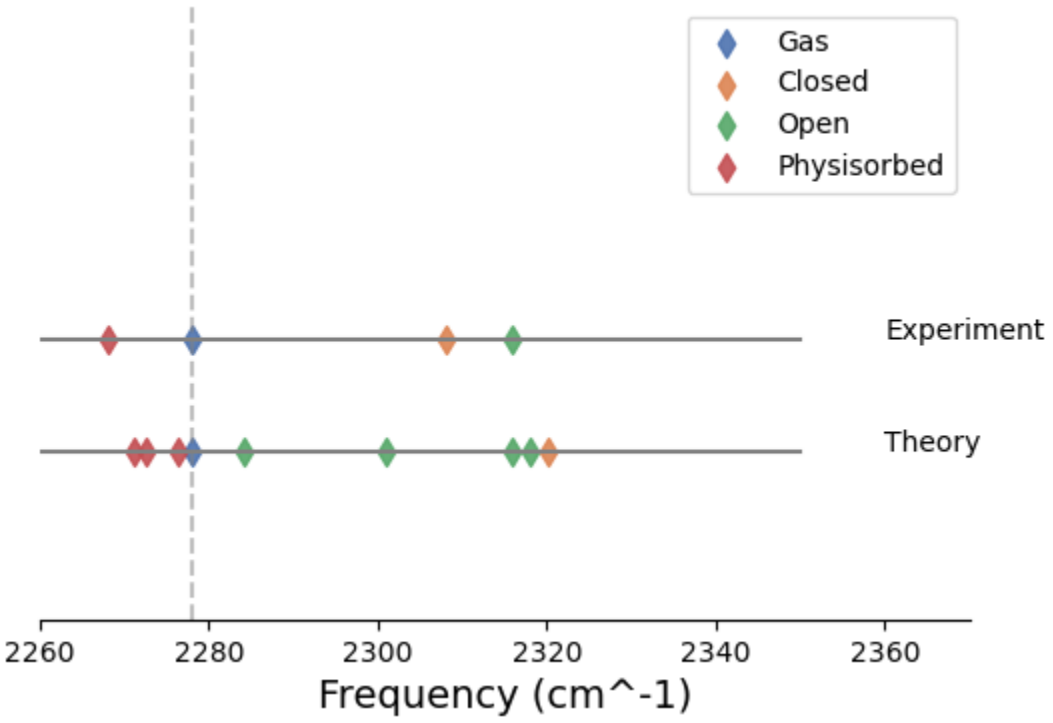

Figure 3. Comparison of experimentally observed CN-stretch frequencies with computed CN-stretch frequencies using a single acetonitrile in the Sn-CHA unit cell.

Next, we broadened our search to include more possible ACN configurations. Since typical ACN loadings outnumber metal atoms in the zeolite, we studied configurations with additional physisorbed ACN, Sn sites with ACN hydrogen bonded to the Sn-OH group, and Sn sites with 2 ACN bound (fig. 4). The 2 ACN bound configurations were unstable, and will not be considered further.

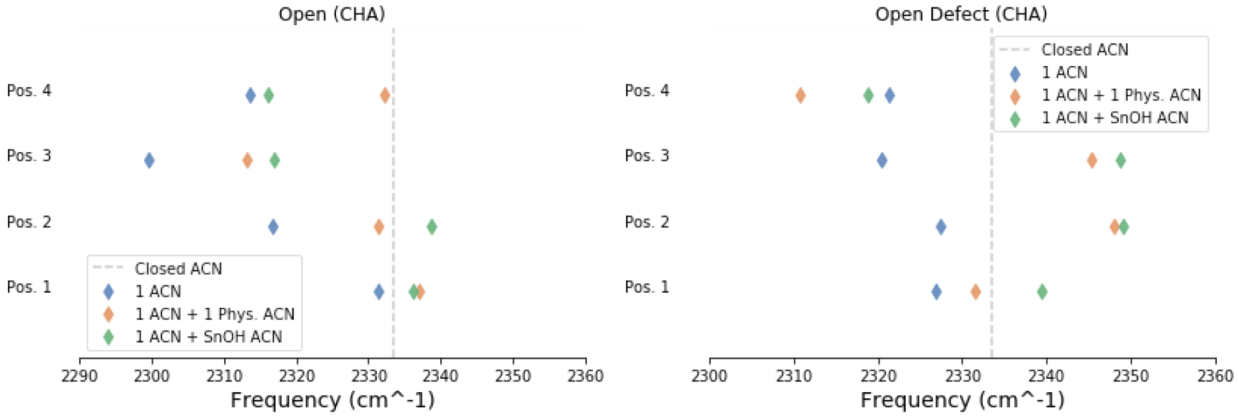

Figure 4. Comparison of CN stretch frequencies for Sn-bound acetonitrile alone (blue), in the presence of physisorbed ACN (orange), and in the presence of ACN coordinated to the SnOH group (green).

The addition of an ACN bound to Sn-OH had a significant effect on the CN stretch and recovered the experimental trend, moving open site vibrations above that of the closed site. This site is physically plausible given the large peak associated with hydrogen bonded ACN in the experimental spectra. This suggests that the additional Sn-OH bonding to open sites is responsible for the open site peaks observed in experiment.

Even for a simple zeolite and small set of configurations, the spread in frequencies in figure 4 is considerable. This creates broad peaks in experimental spectra, making them difficult to interpret, requiring deconvolution to infer active site speciation.

With an understanding of the configurations that contribute to the IR peaks, we can now explain why each peak tends to shift at higher ACN loadings. For each configuration, we computed the binding energy of the Sn-bound acetonitrile (see methods section). Figure 5 demonstrates a clear connection between binding energy and IR frequency. As acetonitrile loading increases, the acetonitrile molecules should bind the most favorable sites first, moving to weaker binding sites only at higher loadings. As loading increases, the acetonitrile peak should shift to lower frequencies, which is also observed in experiment.

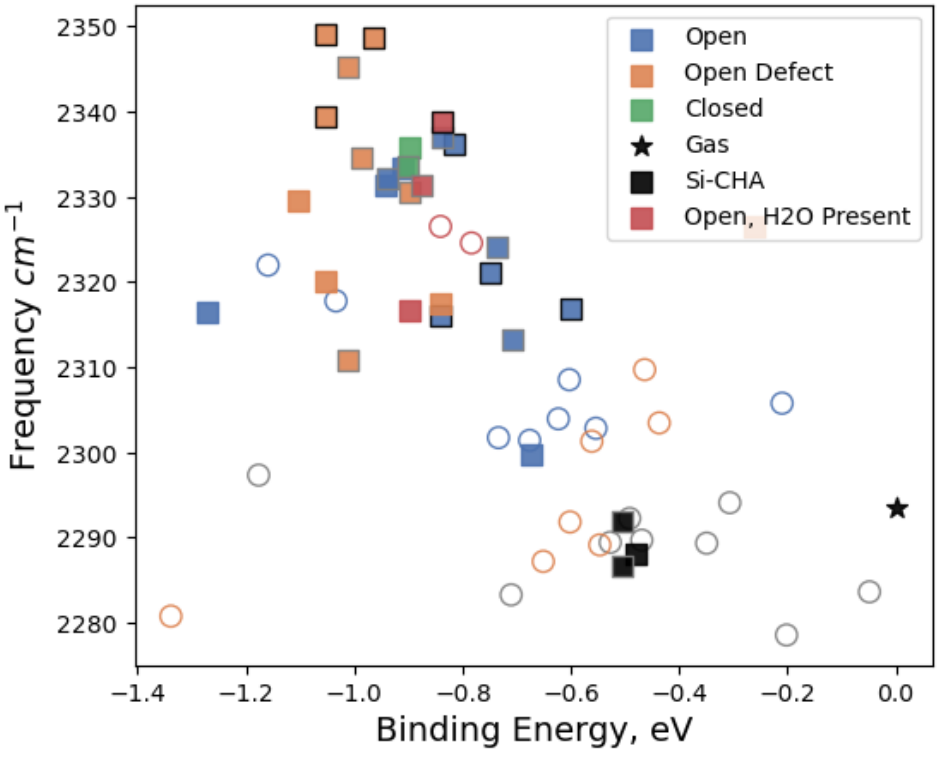

Figure 5. CN stretch frequency vs. binding energy for all configurations. Colored squares denote Sn-bound ACN. Empty circles indicate non-bound ACN. Black borders indicate a hydrogen-bonded ACN is also present.

Leveraging our understanding of the configurations that produce experimental IR spectra, we assessed the viability of a new technique to probe Sn active sites using acetonitrile. Inspired by the common use of ^{15}N NMR probes to characterize zeolites, we examined ACN as an solid state, MAS-NMR probe.

We computed NMR shifts for all relevant species shown in figure 6. Hydrolyzed open and open defect sites differ considerably in their NMR shifts, while the closed sites reside in between them.

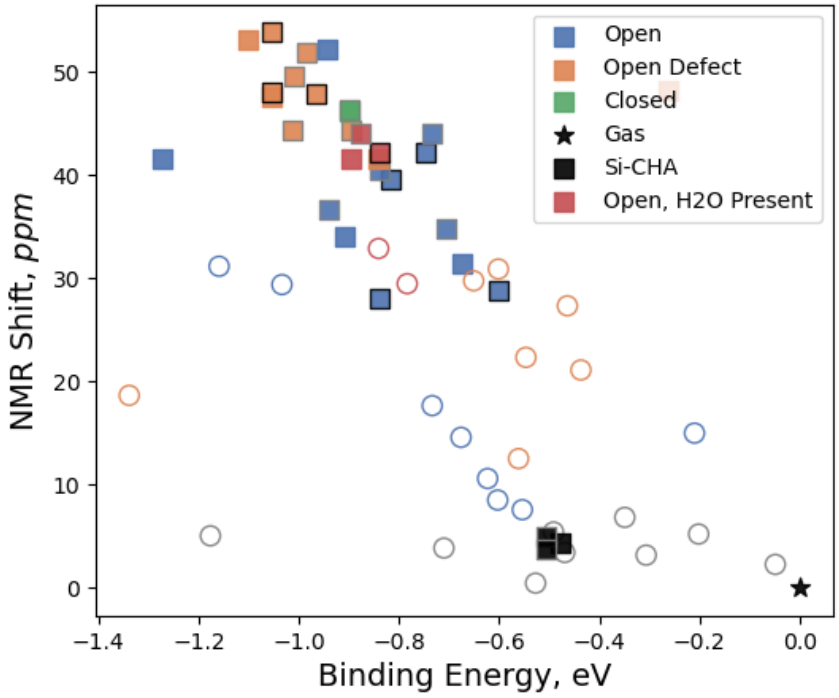

Figure 6. ^{15}N-ACN Isotropic Shift vs. Binding energy. Gas phase ACN referenced to zero.

Peak location is just one piece of information that can be obtained from solid state NMR experiments. Analysis of the peak shape can be used to determine skew and span, each of which

are associated with the geometry of the environment around the NMR nucleus. These parameters can also be straightforwardly computed in a VASP NMR calculation. We examined whether nuclear span can provide additional characterization of Sn site speciation. The nuclear skew results show interesting trends, but their values appear much higher than what is expected experimentally.

Figure 4a illustrates the binding energy trend of nuclear span. Once again, open, open defect, and closed sites exhibit relatively distinct properties. By comparing nuclear shift and span on a single plot in figure 4b, we observe that open and open defect sites cluster into distinct regions.

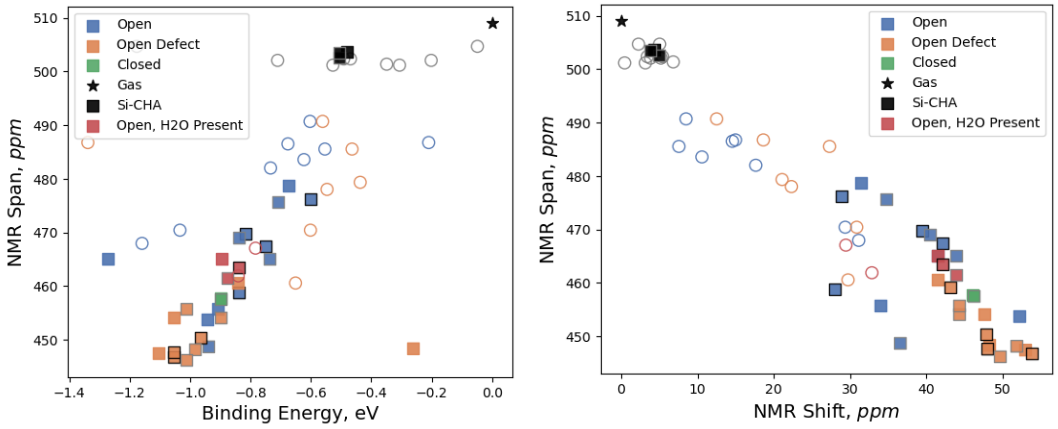

Figure 7. Nuclear Span vs. Binding Energy (left). Isotropic Shift vs. Nuclear Span (right)

Discussion

The IR study confirms that the presence of acetonitrile frequencies above the closed site frequency indicates that open sites are present. Acetonitrile molecules hydrogen bonded to the

OH of the open site significantly affect the frequency of the Sn-bound ACN and contribute to the open site peak.

The CN stretch exhibits a clear dependence on binding energy, with frequency decreasing as binding energy decreases. This helps to explain the increase in the closed site peak at higher ACN loadings. As more ACN is added, the molecules fill lower binding energy sites such as closed sites, resulting in a peak that increases with higher loadings.

The computed vibrational frequencies for Open and Open Defect sites have considerable variance. This suggests that while IR can be used to detect the presence of open sites, it may be difficult to deconvolute different open site peaks to quantify Sn speciation.

By contrast, ^{15}N acetonitrile NMR provides better separation of open sites leading to improved peak deconvolution. NMR can also provide additional information about the local environment of the probe such as the nuclear span which can be used to further differentiate Sn speciation.

Methods

Preparing DFT Structures

To prepare the CHA structure, the Si-CHA crystal structure was obtained from the IZA database. The unit cell was optimized with PBE at 600eV energy cutoff using the gamma point. Keeping the unit cell fixed for the remainder of the study Sn-CHA was produced by replacing an Si atom with an Sn atom. The open sites were produced by adding a water molecule to the structure and positioning the OH group at the most stable location. For the defect open sites, an Si atom

adjacent to the Sn was removed and the resulting unsaturated oxygen atoms were capped with hydrogen atoms. These structures were then optimized at 600 eV energy cutoff. This cutoff was chosen based on the convergence of vibrational frequencies at higher encut. 300 eV and 400 eV ENCUT runs gave significantly different results. Next, the listed ACN configurations were prepared and optimized using the same criteria.

IR Computation

To compute CN stretch frequencies, unconstrained vibration of the entire unit cell was used to avoid errors produced by artificially constraining the lattice. This resulted in many frequencies; to pinpoint the associated CN stretch, all vibrations within a plausible range were visualized. In all cases, there was a unique frequency that displayed a significant CN displacement, and this frequency was reported (full hessian included in the SI).

NMR Computation

To compute nuclear isotropic shielding , the ORCA package was used. 5T cluster models of the Sn active sites were prepared from their periodic structures using the MAZE package. The capping hydrogens were allowed to relax while the other atoms remained fixed. Before computing nuclear isotropic shielding, the peripheral hydrogen, oxygen, and silicon atoms were held fixed while the Sn atom, acetonitrile molecules, and adjacent oxygen atoms were allowed to relax. The peripheral atoms are fixed in order to mimic the rigidity and retain the shape of the periodic structure. Finally, nuclear isotropic shieldings are computed for all N15 atoms.

Conclusion

We analyze the IR spectrum of ACN in Sn-CHA and confirm that the 2316 cm^{-1} peak is indicative of the presence of open sites. However, the spread in frequencies between hydrolyzed open and open defect sites makes peak deconvolution difficult. We propose and theoretically validate ^{15}N ACN as an NMR probe to detect differences in Sn site speciation.

Acetonitrile IR and NMR provide distinct advantages for characterizing Sn zeolites. IR spectroscopy can be completed quickly with low-cost equipment and materials. MAS-NMR requires more expensive equipment and complicated techniques, but can provide new information about tin zeolites. We found that ACN NMR can differentiate Sn sites, and provides additional information about the local environment. As such, ^{15}N ACN NMR is a promising new tool to study Sn speciation in zeolites.

References

(1) Zhang, Q.; Gao, S.; Yu, J. Metal Sites in Zeolites: Synthesis, Characterization, and Catalysis. *Chem. Rev.* **2022**. https://doi.org/10.1021/acs.chemrev.2c00315.

(2) Deshpande, N.; Parulkar, A.; Joshi, R.; Diep, B.; Kulkarni, A.; Brunelli, N. A. Epoxide Ring Opening with Alcohols Using Heterogeneous Lewis Acid Catalysts: Regioselectivity and Mechanism. *J. Catal.* **2019**, *370*, 46–54. https://doi.org/10.1016/j.jcat.2018.11.038.

(3) Vega-Vila, J. C.; Gounder, R. Quantification of Intraporous Hydrophilic Binding Sites in Lewis Acid Zeolites and Consequences for Sugar Isomerization Catalysis. *ACS Catal.* **2020**, *10* (20), 12197–12211. https://doi.org/10.1021/acscatal.0c02918.

(4) First Principles, Microkinetic, and Experimental Analysis of Lewis Acid Site Speciation during Ethanol Dehydration on Sn-Beta Zeolites. *J. Catal.* **2018**, *365*, 261–276. https://doi.org/10.1016/j.jcat.2018.07.012.

(5) Ripmeester, J. A. Surface Acid Site Characterization by Means of CP/MAS Nitrogen-15 NMR. *J. Am. Chem. Soc.* **1983**, *105* (9), 2925–2927. https://doi.org/10.1021/ja00347a083.

(6) Gunther, W. R.; Michaelis, V. K.; Griffin, R. G.; Román-Leshkov, Y. Interrogating the Lewis Acidity of Metal Sites in Beta Zeolites with ^{15}N Pyridine Adsorption Coupled with MAS NMR Spectroscopy. *J. Phys. Chem. C* **2016**, *120* (50), 28533–28544. https://doi.org/10.1021/acs.jpcc.6b07811.

(7) Dib, E.; Mineva, T.; Gaveau, P.; Véron, E.; Sarou-Kanian, V.; Fayon, F.; Alonso, B. Probing Disorder in Al-ZSM-5 Zeolites by ^{14}N NMR Spectroscopy. *J. Phys. Chem. C* **2017**, *121* (29), 15831–15841. https://doi.org/10.1021/acs.jpcc.7b04861.

(8) Harris, J. W.; Liao, W.-C.; Iorio, J. R. D.; Henry, A. M.; Ong, T.-C.; Comas-Vives, A.; Copéret, C.; Gounder, R. *Molecular Structure and Confining Environment of Sn Sites in Single-Site Chabazite Zeolites*. ACS Publications. https://doi.org/10.1021/acs.chemmater.7b03209.

Conclusion

Impacts

This research has important applications for characterizing zeolite active sites. TMPO and acetonitrile NMR can be used to better understand active sites in zeolites both computationally and experimentally. A better understanding of the connection between synthetic conditions and the resulting active site distribution can lead to improved catalyst design.

Evidence for the existence of open defect sites presents new possibilities for active site design. Open defect sites may facilitate certain reactions by organizing the solvent environment, and it may be possible to synthetically address them with new functional groups or metal atoms.

Overall, this work contributes to a better understanding of tin zeolite catalysts, and may facilitate their adaptation to new chemical processes.

Future Work

No research is ever truly complete, and this work could naturally be extended in several ways.

Experiments applying acetonitrile and TMPO NMR probes to other tin zeolites would be a valuable step in validating the technique. Computationally and experimentally, this technique may also provide insights into other Lewis-acid zeolites.

The spin-labeled counterparts of other common IR probes such as CO and NO may also be effective NMR probes, and approaches similar to those used in this work could be used to validate such techniques. More advanced techniques such as two-dimensional NMR spectroscopy may be able to exploit the interactions between NMR probes, spin-active metal atoms, and silanol groups to obtain detailed information about the active site.

It remains an open challenge whether a zeolite containing exclusively defect open Lewis-acid sites can be created in the lab. This would be a significant achievement and may make it possible to add new functional groups to the adjacent silanol nest or insert additional metal atoms into the framework.

The Role of Theory in Catalyst Research: Atomistic Explanations

In each chapter, a similar storyhas unfolded. Experimental data provided an intriguing yet poorly understood pattern, a question that was difficult to answer with characterization alone. My subsequent investigation attempted to enumerate and study all plausible arrangements of the atoms of interest. As is common for DFT, the results usually did not match experiment in a quantitative way, yet the trends across many configurations provided insight into the workings of the catalyst, putting the experimental results in context and suggesting new experiments to be run.

Despite the rigorous mathematics that underlies DFT, the approximations required to model chemical systems make it difficult to obtain quantitative agreement with experiment. But this doesn't prevent computational methods from being useful in catalyst research. Taking inspiration from Deutch's *The Beginning of Infinity,* I claim that the real value of computational methods comes from providing new explanations based on atomistic simulations. Rather than being quantitative, DFT calculations can qualitatively assess different theories in ways that are inaccessible to experiments.

These "atomistic explanations" provide repeatable, explicit, and physically grounded stories about what's really happening in a material. They can guide catalyst design or suggest new experiments to run, complementing other characterization approaches. I hope this way of thinking about simulation will encourage the field to emphasize methods amenable to understanding experimental data, rather than simply agreeing with it.